Published in Journal of Petrology 48, issue 9, 1725-1760, 2007
which should be used for any reference to this work

Crystallization and Breakdown of Metasomatic Phases in Graphite-bearing Peridotite Xenoliths from Marsabit (Kenya)

BENJAMIN KAESER[1]*, ANGELIKA KALT[1] AND THOMAS PETTKE[2]

[1]INSTITUT DE GÉOLOGIE ET D'HYDROGÉOLOGIE, UNIVERSITÉ DE NEUCHÂTEL, RUE EMILE-ARGAND 11, CH-2009 NEUCHÂTEL, SWITZERLAND

[2]INSTITUTE OF GEOLOGICAL SCIENCES, UNIVERSITY OF BERN, BALTZERSTRASSE 1, CH-3012, BERN, SWITZERLAND

Mantle-derived xenoliths from the Marsabit shield volcano (eastern flank of the Kenya rift) include porphyroclastic spinel peridotites characterized by variable styles of metasomatism. The petrography of the xenoliths indicates a transition from primary clinopyroxene-bearing cryptically metasomatized harzburgite (light rare earth element, U, and Th enrichment in clinopyroxene) to modally metasomatized clinopyroxene-free harzburgite and dunite. The metasomatic phases include amphibole (low-Ti Mg-katophorite), Na-rich phlogopite, apatite, graphite and metasomatic low-Al orthopyroxene. Transitional samples show that metasomatism led to replacement of clinopyroxene by amphibole. In all modally metasomatized xenoliths melt pockets (silicate glass containing silicate and oxide microphenocrysts, carbonates and empty vugs) occur in close textural relationship with the earlier metasomatic phases. The petrography, major and trace element data, together with constraints from thermobarometry and fO_2 calculations, indicate that the cryptic and modal metasomatism are the result of a single event of interaction between peridotite and an orthopyroxene-saturated volatile-rich silicate melt. The unusual style of metasomatism (composition of amphibole, presence of graphite, formation of orthopyroxene) reflects low P–T *conditions (~850–1000°C at <1·5 GPa) in the wall-rocks during impregnation and locally low oxygen fugacities. The latter allowed the precipitation of graphite from CO_2. The inferred melt was possibly derived from alkaline basic melts by melt–rock reaction during the development of the Tertiary–Quaternary Kenya rift. Glass-bearing melt pockets formed at the expense of the early phases, mainly through incongruent melting of amphibole and orthopyroxene, triggered by infiltration of a CO_2-rich fluid and heating related to the magmatic activity that ultimately sampled and transported the xenoliths to the surface.*

KEY WORDS: *graphite; peridotite xenoliths; Kenya Rift; modal metasomatism; silicate glass*

INTRODUCTION

During recent decades numerous studies have described different styles of metasomatism in the Earth's upper mantle. These studies, in combination with experimental work, show that the agents responsible for mantle metasomatism include mafic silicate melts, carbonate melts or C–O–H-rich fluids (e.g. reviews by Menzies & Hawkesworth, 1987; Luth, 2003). Integration of textural, mineralogical and geochemical data from mantle samples highlights the complexity of mantle metasomatism. The data show that metasomatic features are controlled by: (1) the composition of the initial metasomatizing agent; (2) the pre-metasomatic composition and heterogeneity of the mantle rock; (3) the evolution of the physico-chemical parameters during metasomatism (e.g. porosity, fO_2, P, T); (4) element fractionation processes during melt (fluid)–rock interaction; (5) mineral reactions. Several recent studies have demonstrated that compositional differences between metasomatic products in a single suite of mantle rocks do not necessarily imply different metasomatizing events (e.g. Bedini *et al.*, 1997; Ionov *et al.*, 2002, 2006; Bodinier *et al.*, 2004; Rivalenti *et al.*, 2004). Processes such as chromatographic fractionation and melt/fluid–rock reaction can generate compositionally distinct products, starting from one initial melt or fluid

*Corresponding author. Present address: School of GeoSciences, University of Edinburgh, West Mains Road, Edinburgh EH9 3JW, UK. Telephone: 0044 (0) 131 650 7339. Fax: 0044 (0) 131 668 3184.
E-mail: v1bkaser@staffmail.ed.ac.uk

(e.g. Navon & Stolper, 1987; Harte *et al.*, 1993; Godard *et al.*, 1995; Vernières *et al.*, 1997).

We present a study of metasomatized, graphite-bearing xenoliths from Marsabit (northern Kenya), to investigate melt–rock reaction and fractionation processes. The products of metasomatism are texturally and compositionally variable and unusual. An early Na–Si-rich assemblage comprises volatile-bearing phases (amphibole, phlogopite, apatite) and metasomatic orthopyroxene, as well as graphite. Associated with these phases is a second metasomatic assemblage of carbonate-bearing silicate glass patches ('melt pockets'), similar to those described from many other xenolith suites (e.g. Frey & Green, 1974; Dautria *et al.*, 1992; Ionov *et al.*, 1993, 1994; Zinngrebe & Foley, 1995; Chazot *et al.*, 1996*a*; Draper & Green, 1997; Yaxley *et al.*, 1997; Coltorti *et al.*, 2000; Laurora *et al.*, 2001; Bali *et al.*, 2002; Ban *et al.*, 2005). Our approach is based on detailed investigation of trace element variation in minerals and integration of textural constraints. It emphasizes that the 'exotic' nature of the metasomatic products reflects a particular pre-existing physical and chemical environment—i.e. low ambient temperatures (and probably pressures) and relatively low oxygen fugacities—rather than an exotic initial metasomatic agent. We will show that metasomatism in this case does not necessitate multiple metasomatic events of different nature, but simply reflects the product of melt–rock reaction, possibly initiated by common, continental rift-related basanites. We further present mass-balance calculations, which show that the melt pockets were formed by *in situ* partial melting of the early assemblage (mainly amphibole and orthopyroxene), triggered by infiltration of a CO_2-rich fluid.

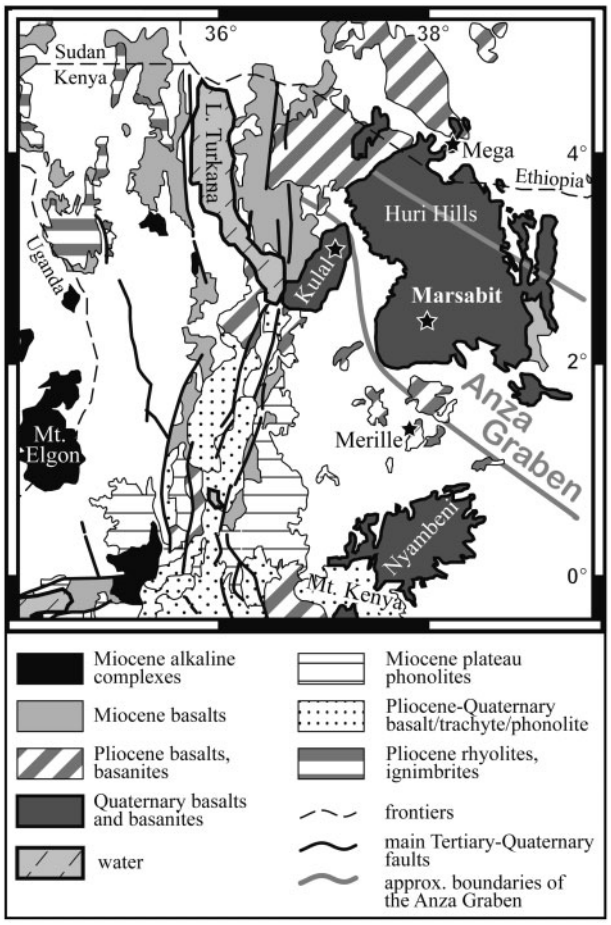

Fig. 1. Simplified geological map showing the distribution of volcanic rocks associated with the Kenyan sector of the East African rift system; compiled on the basis of the maps of King (1970) and Baker *et al.* (1971). Stars indicate other off-craton xenolith localities (Henjes-Kunst & Altherr, 1992; Bedini *et al.*, 1997). The approximate position of the Anza Graben is taken from Henjes-Kunst & Altherr (1992).

SAMPLE CONTEXT

The investigated mantle xenoliths were collected from scoriae of basanitic to alkali-basaltic Quaternary cinder cones of the Marsabit shield volcano (Volker, 1990; Henjes-Kunst & Altherr, 1992). Magmatic activity in Marsabit started in the late Miocene, whereas rocks from the shield volcano yield Pleistocene to Quaternary ages (e.g. Key *et al.*, 1987). Magmatism is thus clearly related to the development of the Kenya rift (i.e. the eastern branch of the East African Rift system, EARS; see Fig. 1). The Marsabit shield volcano is, however, located eastward of the main axis of the EARS, within the Anza Graben, the eastward continuation of the Turkana depression. The evolution of the lithosphere in this region includes multiple accretion during Pan-African orogenesis (formation of the Pan-African Mozambique belt from 720 to 550 Ma; e.g. Meert, 2003), followed by several phases of continental rifting, including formation of the Mesozoic–Paleogene Anza Graben, later cross-cut by the Tertiary–Quaternary EARS [see Fig. 1 and Morley (1999) for a review]. A more detailed description of the geological and geodynamic context has been given by Kaeser *et al.* (2006).

In our previous study (Kaeser *et al.*, 2006) we used the Marsabit peridotite xenoliths to constrain the evolution of the lithospheric mantle beneath Marsabit. The peridotites were subdivided into four groups, including the porphyroclastic spinel harzburgites and dunites (Group III) investigated here (Table 1). For detailed descriptions of the textures and mineral chemistry of the primary assemblages of all four groups the reader is referred to Kaeser *et al.* (2006).

Thermobarometry calculations revealed that all the porphyroclastic rocks experienced decompression and cooling from high pressures and temperatures

Table 1: Textures and mineralogical composition of the investigated peridotite xenoliths

Sample no.	Type	Lithology	Pre-metasomatic and early metasomatic phases (vol.%)								Melt pockets	Modal composition of melt pockets					
			Former garnet[1]	Ol	Opx	Cpx	Spl	Am	Phl	Graphite/ apatite		Glass	Di_m	Ol_m	Chr_m	Mg-Cc	Vugs
Ke 1965/1	III-a	porphyroclastic spl harzburgite	1·5	70·8	22·9	3·9	0·9	—	—	tr./—	—	—	—	—	—	—	—
Ke 1959/15	III-b	porphyroclastic spl harzburgite	5·0	63·0	26·0	5·2	0·7	0·2	—	—/tr.	<4·0	21·8	23·4	27·7	4·9	8·1[2]	7·6
Ke 1965/15	III-b	porphyroclastic spl harzburgite	—	71·9	17·7	6·8	0·4	0·2	0·1	0·10/tr.	3·0	21·4	34·0	23·7	2·8	16·0	2·2
Ke 785*	III-c	porphyroclastic spl harzburgite	—	64·0	18·7[3]	—	0·6[4]	1·1	0·9	0·23/—	14·4	21·9	27·0	21·8	5·7	6·7	7·0
Ke 1965/3	III-c	porphyroclastic spl dunite	—	80·1	3·2[3]	—	0·7[4]	—	tr.	—/tr.	16·0	22·7	21·3	29·5	6·6	12·8[5]	7·4
Ke 1965/25	III-c	porphyroclastic amphibole dunite	—	53·6	—	—	—	12·0	tr.	0·25/—	34·2	n.d.	n.d.	n.d.	n.d.	n.d.	n.d.
Ke 1959/27	III-c	porphyroclastic dunite	—	88·5	tr.[3]	—	—	—	—	—	11·5	n.d.	n.d.	n.d.	n.d.	n.d.	n.d.
Ke 1970/6	III-d	recrystallized spl harzburgite	—	87·2	9·5[3]	2·7[6]	0·6[4]	—	—	—	—	—	—	—	—	—	—

Ol, olivine; Opx, orthopyroxene; Cpx, clinopyroxene; Am, amphibole; Phl, phlogopite; Di_m, Ol_m, Chr_m, diopside, olivine and chromite micro-phenocrysts in melt pockets; Mg-Cc, Mg-calcite. [1]Spl–opx–cpx symplectites. [2]Dolomite instead of calcite. [3]Metasomatic, low-Al orthopyroxene (Opx_m). [4]Compositionally identical to Chr_m. [5]Highly variable (2·4–19·7 vol.%) in individual melt pockets. [6]Compositionally similar to glass-related Di_m. —, not detected; tr., traces; n.d., not determined.

(mainly preserved in formerly garnet-bearing Group I lherzolites; see Fig. 2) to low mantle P–T conditions of <900°C at <1·5 GPa (Kaeser *et al.*, 2006). The present study focuses on metasomatic features in the low-temperature Group III xenoliths. Textural and compositional characteristics suggest a genetic relationship with late EARS-related heating and cryptic metasomatism, leading to U–Th–Nb and light rare earth element (LREE) enrichment in clinopyroxene in the recrystallized Group II lherzolites. The latter were interpreted to reflect metasomatism by percolation of alkaline mafic melts, possibly parental to the Quaternary magmas of the Marsabit volcano (Kaeser *et al.*, 2006), post-dating rift-related decompression and deformation. In contrast, metasomatic phases in the porphyroclastic Group I lherzolites (i.e. Ti-pargasite and rare phlogopite; Kaeser *et al.*, 2006) are texturally and compositionally distinct, suggesting a different event. The trace element signatures of Ti-pargasite suggest that this metasomatic assemblage formed earlier, prior to rift-related decompression and deformation (Kaeser *et al.*, 2006).

ANALYTICAL METHODS

Modal compositions (Table 1) were determined from digitized images of thin sections and rock slice scans (for details, see Kaeser *et al.*, 2006). Minerals were analysed for major elements using a CAMECA SX 50 electron microprobe equipped with four wavelength-dispersive spectrometers (Mineralogisch-Petrographisches Institut, Universität Bern) and a CAMECA SX 51 electron microprobe with five wavelength-dispersive spectrometers (Mineralogisches Institut, Universität Heidelberg). Pyroxene, olivine and spinel were analysed using routine operating conditions (focused beam, accelerating voltage of 15 kV, beam current of 20 nA, and counting times of 20 s for most elements). Silicate glass was analysed with a larger beam size (~10–15 μm) and a lower beam current (15 nA) to avoid Na loss during analysis. Natural and synthetic silicates and oxides were used as standards. Carbonates were analysed with a beam current of 10 nA and a beam size of 10 μm, using natural carbonates and sulfates as standards. The concentrations of CO_2 (in carbonates) and Fe^{3+} (in spinel) were calculated

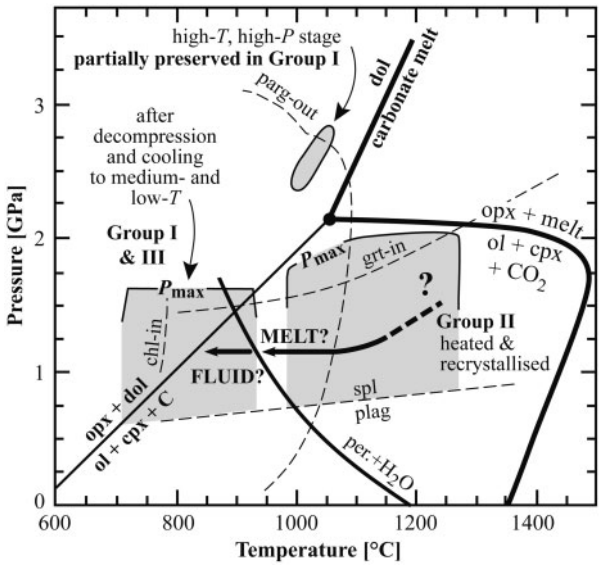

Fig. 2. Pressure–temperature evolution recorded by peridotite xenoliths from Marsabit (light grey fields; summarized from Kaeser *et al.*, 2006), together with reactions relevant for this study: plagioclase–spinel transition in the CFMAS system (Gasparik, 1987); appearance of garnet (grt) in model lherzolite (Klemme & O'Neill, 2000); maximum stability of Ti-pargasite (parg) in model lherzolite (Niida & Green, 1999); appearance of chlorite (chl) in model lherzolite under fluid-saturated conditions (Fumagalli & Poli, 2005); solidus for primitive mantle under water-saturated conditions (per. + H_2O; Grove *et al.*, 2006); solidus of natural carbonated lherzolite from Lee & Wyllie (2000); subsolidus decarbonation (opx + dol = ol + cpx + C) from Woermann & Rosenhauer (1985) at fO_2 below the carbon–carbon oxide (CCO) buffer. The bold arrow schematically indicates the infiltrating and cooling metasomatizing Si-rich melt at supersolidus and derivative fluid at subsolidus conditions. (See text for further explanation.)

based on stoichiometry. The raw data of all microprobe analyses were corrected using routine PAP software.

Trace element contents in minerals were analysed *in-situ* on polished thin sections (40–50 μm thick), using a laser ablation (LA) instrument equipped with a 193 nm ArF excimer laser (Lambda Physik, Germany) coupled to an ELAN 6100 (Perkin Elmer, Canada) quadrupole inductively coupled plasma mass spectrometer (ICPMS) at the Institut für Isotopengeologie und Mineralische Rohstoffe, ETH Zürich [see Pettke *et al.* (2004) and references therein for the instrumental setup, capabilities and operating conditions]. Raw data were reduced using the LAMTRACE program. Laser pit diameters were between 14 and 110 μm, depending on grain size and the absence or presence of mineral, fluid or melt inclusions, and of exsolution lamellae.

PETROGRAPHY

Group III harzburgites and dunites display two texturally different types of modal metasomatic modification. The first type of metasomatism formed clusters and veinlets of volatile-bearing minerals (amphibole, phlogopite, ± graphite, ± apatite; Fig. 3a–e), associated with metasomatic orthopyroxene. The second type is characterized by the occurrence of 'melt pockets' (e.g. Frey & Green, 1974; Ionov *et al.*, 1994): patches and networks of silicate glass associated with microphenocrysts of clinopyroxene, olivine and chromite (Fig. 4a–f). Glass further contains globules of carbonates and vugs (Figs 4a–e and 5a, b). Melt pockets form at least partly at the expense of volatile-bearing minerals. Therefore, the volatile-bearing assemblage is referred to in the following as 'early metasomatic' (including metasomatic orthopyroxene referred to as Opx_m). The later glass-bearing assemblage is termed 'late metasomatic' (Na-rich Cr diopside, Di_m; olivine, Ol_m; chromite, Chr_m). The pre-metasomatic peridotitic phases are termed 'primary' (olivine, ol-I; clinopyroxene, cpx-I; orthopyroxene, opx-I; spinel, spl-I).

Based on petrographic investigations, we subdivided Group III peridotites into four types (Type III-a to -d). Textural and geochemical features show that the transition from Type III-a to Type III-c (+d) mainly corresponds to the transformation of modally non-metasomatized spinel harzburgite to pervasively overprinted amphibole harzburgite–dunite. Twenty out of 27 Group III samples investigated petrographically show evidence for modal metasomatism (i.e. they belong to Type III-b or -c).

Type III-a

Type III-a is classified as porphyroclastic, cpx-I-bearing spl harzburgite, devoid of volatile-bearing phases, but showing geochemical evidence of cryptic metasomatism (Kaeser *et al.*, 2006, and this study). This rock type was originally garnet-bearing and was subjected to decompression, as is indicated by the presence of rare spl–opx–cpx symplectites (Table 1 and Kaeser *et al.*, 2006).

Type III-b

Xenoliths of Type III-b are cpx-I-bearing spinel harzburgites; however, they contain metasomatic volatile-bearing phases (Table 1). One xenolith (Ke 1965/15) contains veinlets of pale green amphibole, phlogopite, graphite ± apatite (Figs 3e and 4b). Graphite occurs as macroscopic flakes (up to 500 μm long; Fig. 3e), similar to those described from cratonic, kimberlite-hosted peridotite xenoliths (Pearson *et al.*, 1994). Cpx-I in the vicinity of veinlets is strongly resorbed and develops patches or lamellae of Ti-poor amphibole, indicating metasomatic replacement (Fig. 4b). In all Type III-b samples amphibole and clinopyroxene are partially replaced by the late glass-bearing assemblage (e.g. Fig. 4a). Cpx-I is overgrown by a secondary, green Na-rich Cr diopside (Di_m) occasionally containing fluid, glass and/or carbonate inclusions (Fig. 2c). Di_m further occurs as micro-phenocrysts in melt pockets, sometimes enclosing (resorbed?) orthopyroxene.

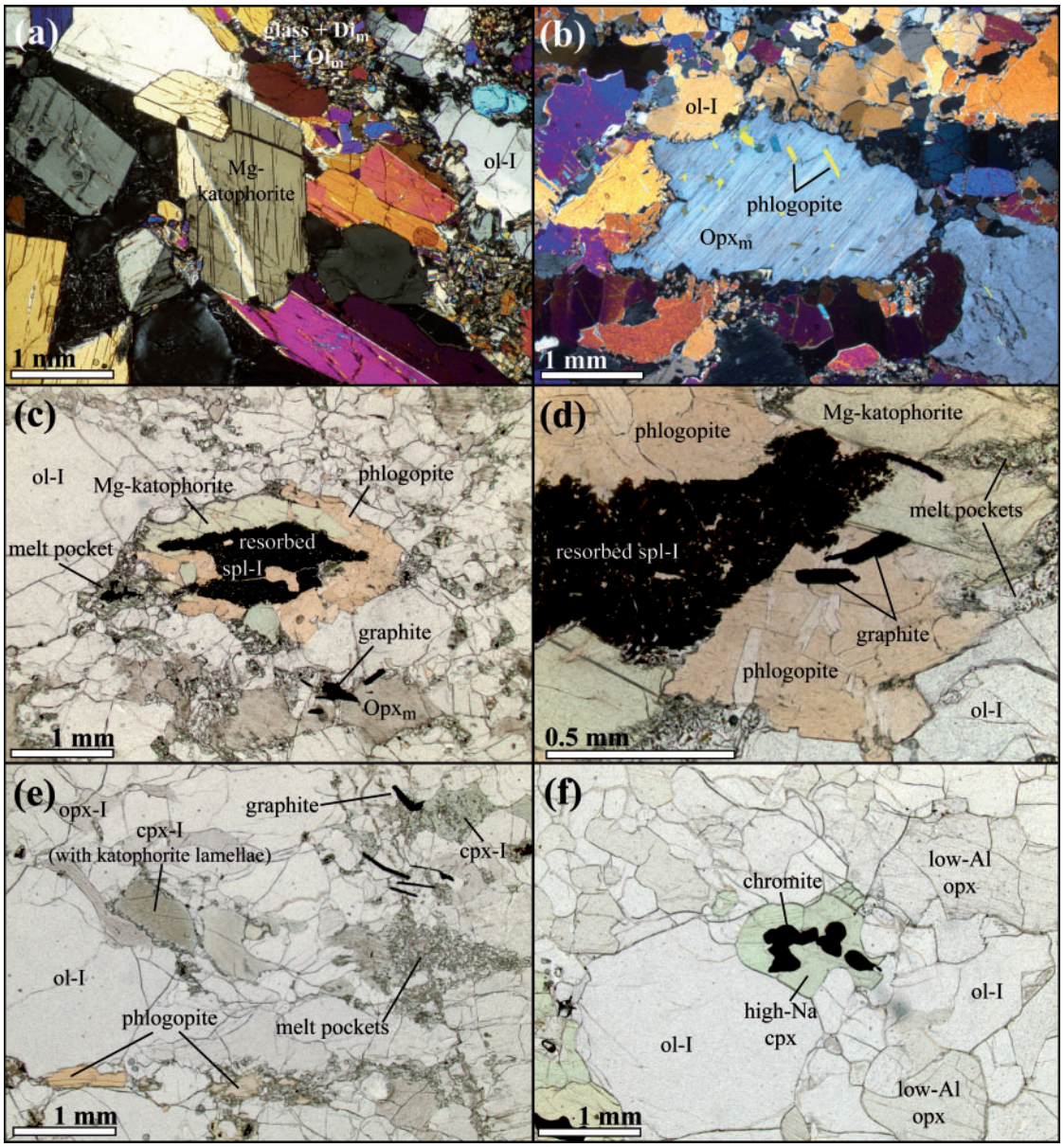

Fig. 3. Photomicrographs showing the textural characteristics of metasomatism in the porphyroclastic spinel harzburgites and dunites from Marsabit. (a) Twinned, euhedral Mg-katophorite in Type III-c amphibole dunite. The irregular grain boundaries with glass + microlite-bearing melt pockets should be noted (sample Ke 1965/25; crossed polars). (b) metasomatic low-Al orthopyroxene (Opx_m) in a Type III-c spinel harzburgite with euhedral phlogopite inclusions (early metasomatic assemblage). Irregular, concave grain boundaries indicating later resorption by olivine should be noted (sample Ke 785*; crossed polarizers). (c) Type III-c Mg-katophorite and phlogopite clustering around partly resorbed spinel (spl-I), and metasomatic orthopyroxene (Opx_m) in contact with partly included graphite (sample Ke 785*). (d) Details of Type III-c early metasomatic Mg-katophorite and phlogopite, the latter containing graphite inclusions (sample Ke 785*). (e) Type III-b early metasomatic assemblage including interstitial phlogopite, graphite and clinopyroxene (cpx-I) becoming replaced by Mg-katophorite lamellae (sample Ke 1965/15). (f) Type III-d spl harzburgite characterized by annealed textures and clusters of chromite enclosed by green Na-rich clinopyroxene (cpx; sample Ke 1970/6).

Type III-c

Type III-c samples are harzburgites and dunites devoid of cpx-I. Samples transitional between Type III-b and -c still contain relics of cpx-I. Metasomatic products in Type III-c xenoliths generally occur as clusters of amphibole, phlogopite, graphite and rare apatite. The primary assemblage is dominated by ol-I. Green, Ti-poor amphibole and phlogopite typically form aggregates around relic, skeletal spl-I (Fig. 3c and d). Dunite xenolith Ke 1965/25 is unusual as it contains centimetre-scale clusters of large,

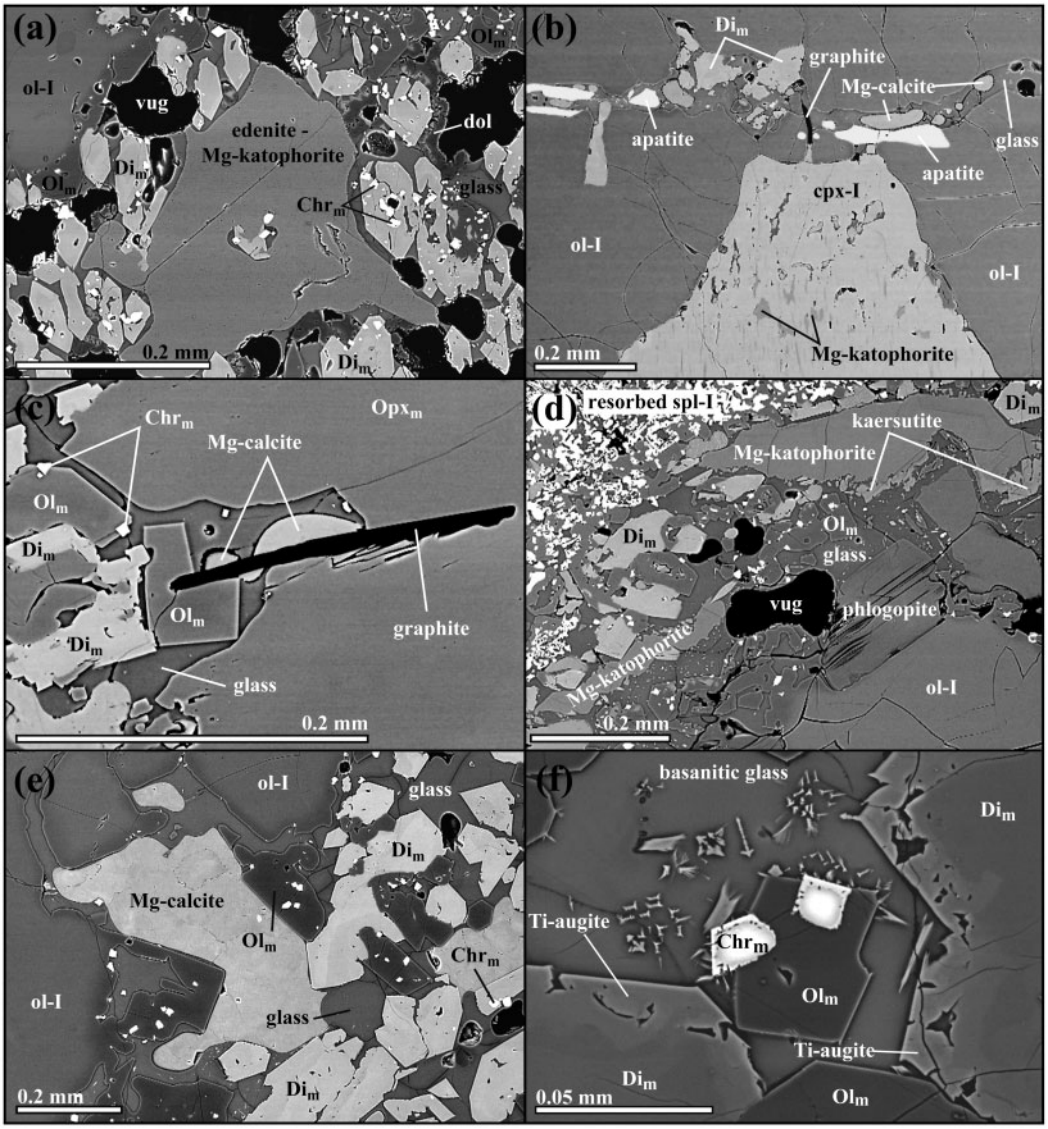

Fig. 4. Back-scattered electron images showing textural characteristics and relationships between early and late metasomatic assemblages. (a) Relic amphibole (edenite–Mg-katophorite) in a typical melt pocket containing clinopyroxene (Di_m), olivine (Ol_m) and chromite (Chr_m) micro-phenocrysts, as well as silicate glass with vugs (sometimes lined or filled with dolomitic carbonate (Type III-b xenolith Ke 1959/15). (b) Type III-b spinel harzburgite showing the textural characteristics of early (graphite, apatite, Mg-katophorite replacing cpx-I) and late (glass, Mg-calcite, Di_m) metasomatic assemblages (sample Ke 1965/15). (c) Formation of glass and micro-phenocrysts (Ol_m and Di_m) at the expense of metasomatic orthopyroxene (Opx_m). It should be noted also that graphite is overgrown by Mg-calcite when no longer in contact with Opx_m (Type III-b spinel harzburgite Ke 1965/15). (d) Phlogopite and residual Mg-katophorite in a melt pocket in a Type III-c spl harzburgite. The more regular grain boundaries of phlogopite compared with Mg-katophorite should be noted (the latter is further rimmed by irregular kaersutitic amphibole; sample Ke 785*). (e) Silicate glass, Mg-calcite and microlites of Na-rich Cr diopside (Di_m), olivine (Ol_m), and chromite (Chr_m) in a Type III-c spinel harzburgite. The grey tone variation in Di_m, indicating zoning, should be noted (sample Ke 1965/3). (f) Host-related basanitic glass (containing minute clinopyroxene quench crystals) in the peculiar Type III-c xenolith Ke 1959/27. The Ti-augite reaction rims on Na-rich Cr diopside (Di_m) micro-phenocrysts and the resorbed grain boundaries of chromite (Chr_m) should be noted.

euhedral twinned amphibole crystals (Fig. 3a) with small phlogopite inclusions. Graphite is associated with amphibole and phlogopite (sometimes found as inclusions in the latter; Fig. 3d) or orthopyroxene (Fig. 3c). Straight contacts between amphibole, phlogopite and ol-I indicate textural equilibrium. Phlogopite also occurs as euhedral, randomly dispersed flakes in orthopyroxene (Fig. 3b). This, together with compositional arguments (e.g. very low Al contents; see below), suggests that orthopyroxene is related to metasomatism (Opx_m). Sample Ke 1965/3 also contains early metasomatic interstitial apatite.

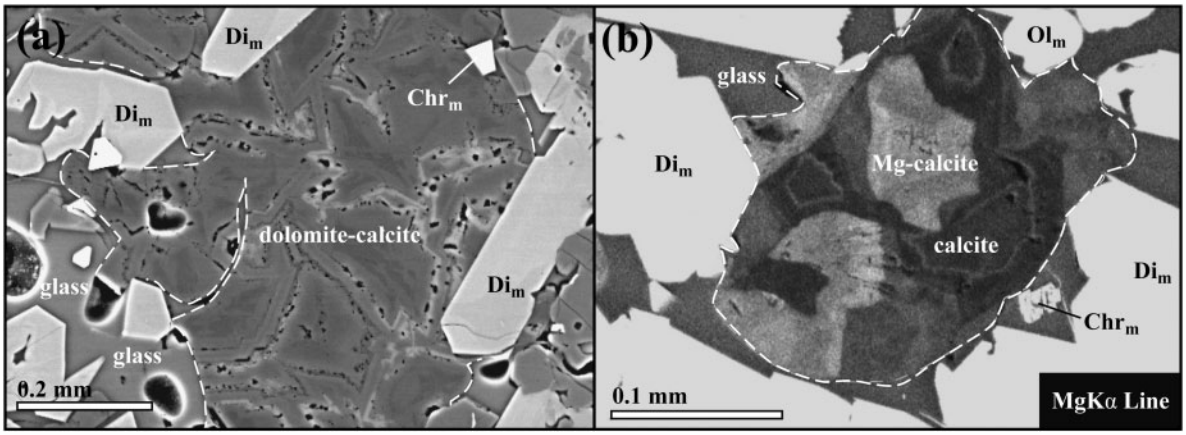

Fig. 5. Oscillatory zoning of carbonate related to silicate glass in porphyroclastic spinel harzburgites from Marsabit. (a) Zoned, euhedral dolomite crystals (dark) rimmed by fine selvages of calcite (light), together with Na-rich Cr diopside (Di_m) and chromite (Chr_m; sample Ke 1959/15). (b) Qualitative compositional map of carbonates in a melt pocket (sample Ke 1965/3). Lighter grey tones indicate higher Mg contents. The euhedral shapes of the carbonate crystals should be noted. The dashed white lines in (a) and (b) highlight the contact of carbonates with the pristine silicate glass.

Late metasomatic assemblages are ubiquitous in Type III-c xenoliths. They form melt pockets, interconnected by glass films along olivine grain boundaries. Euhedral apple-green Na-rich Cr diopside micro-phenocrysts (Di_m; up to 0·3 mm long) in individual melt pockets commonly have the same crystallographic orientation (Fig. 4a), suggesting growth at the expense of an earlier phase. Back-scattered electron (BSE) imaging reveals patchy zoning (Figs 4e and 5a). Melt pockets in several samples enclose relic, resorbed amphibole grains (Fig. 4d). Phlogopite (e.g. in Ke 785*) appears to be less resorbed (Fig. 4d). Early amphibole is rimmed by a kaersutitic selvage (Fig. 4d), indicating that the early amphibole is not in chemical equilibrium with the silicate glass. When in contact with glass, Opx_m is also strongly resorbed. Several features suggest incongruent breakdown by a process similar to the reaction opx + melt → ol + cpx + modified melt (e.g. Shaw *et al.*, 1998): thin glass films are present on orthopyroxene cleavage planes, late euhedral $Ol_m + Di_m \pm Chr_m$ nucleated within orthopyroxene and Ol_m overgrows orthopyroxene (Fig. 3b; development of strongly concave opx grain boundaries).

Glass in Type III-b and -c samples contains considerable amounts of rounded carbonates (e.g. Figs 4e and 5a), texturally similar to interstitial, glass-related carbonate globules from other xenolith suites (e.g. Ionov *et al.*, 1993, 1996; Norman, 1998; Lee *et al.*, 2000; Laurora *et al.*, 2001; Bali *et al.*, 2002; Demény *et al.*, 2004). BSE imaging and qualitative energy-dispersive spectrometry mapping highlight that carbonate globules consist of clusters of sometimes euhedral Mg-calcite or dolomite crystals, occasionally showing oscillatory zoning (Fig. 5a and b). In sample Ke 1965/15, Mg-calcite is in contact with graphite flakes (Fig. 4c), indicating nucleation of carbonate on graphite. Glass in several samples contains rounded blebs of apatite (Fig. 4b), as well as minor amounts of Fe–Ni sulphide globules. Abundant vugs (e.g. Fig. 4a and d) in all types of silicate glass are possibly remnants of an exsolved vapour phase.

Sample Ke 1959/27 (Type III-c) is unusual in several aspects. It contains kaersutite phenocrysts hosted in the glass. Further, Di_m micro-phenocrysts are overgrown by Ti-augite rims (Fig. 4f), and the glass is of an untypical dark brown colour. This xenolith records interaction with a melt similar to the host basanite during ascent to the surface.

Type III-d

Type III-d is a unique sample (Ke 1970/6) of metasomatic coarse-grained spinel harzburgite (grain size ≤4 mm; Fig. 3f). Olivine and orthopyroxene are almost strain free. Spinel occurs as rounded, black grains (chromite) surrounded by a cluster of apple-green Na-rich Cr diopside (Fig. 3f) containing glass inclusions. Volatile-bearing phases are absent. Several orthopyroxene grains show numerous melt inclusions forming continuous films or trails along cleavage planes. These remarkable textural features can be explained by almost complete annealing of a former Type III-c spinel harzburgite containing silicate glass + Di_m micro-phenocrysts, which subsequently recrystallized to form the clinopyroxene clusters around spinel and orthopyroxene with melt inclusions.

MINERAL COMPOSITION

Compositional data (major and trace elements) for non-metasomatic primary phases from all peridotite types, as well as for Ti-pargasite and phlogopite from Group I samples have been given by Kaeser *et al.* (2006). A more complete dataset with respect to the metasomatic phase assemblages discussed in this paper is available at http://petrology.oxfordjournals.org.

Early metasomatic assemblages

Clinopyroxene

'Cryptically' metasomatized cpx-I (Type III-a and -b) are diopsides (Table 2) with high Mg-numbers and low Ti contents typical for mantle harzburgite (e.g. Pearson *et al.*, 2003). The major element compositions of 'unmetasomatized' cpx-I from Type III-a and -b xenoliths are similar. However, Type III-b samples occasionally contain clinopyroxene that is texturally identical to cpx-I but contains significantly higher amounts of Na_2O (up to 2·54 wt%; see Fig. 6a), pointing to cryptic metasomatism. Trace element analyses (Table 2) show enrichment of U, Th, Sr, and LREE relative to middle REE (MREE), variable depletions in heavy REE (HREE), and marked negative anomalies for high field strength elements (HFSE; Nb, Ta, Zr, Hf, Ti; Fig. 7a). Trace element enrichment is strongest in the high-Na cpx-I (Fig. 7a).

Orthopyroxene

Opx-I from Type III-a and -b xenoliths is enstatite-rich (Mg-number of 91·2–92·5). It is LREE-depleted and slightly enriched in U and Th, indicating cryptic metasomatism (Table 3). Opx_m (Types III-c and -d) has higher Mg-numbers than opx-I (up to 93·1) and is extremely Al-poor (0·2–1·0 wt% Al_2O_3). LREE and MREE are slightly enriched relative to HFSE, which is unusual for mantle-derived orthopyroxene (Rampone *et al.*, 1991).

Amphibole

Green amphibole (Type III-b and -c) is mostly Ti-poor (Table 4) with very high Si and Na contents and high Mg-numbers (Fig. 8a and b). Low-Ti amphibole in Type III-c is Mg-katophorite (Fig. 8a; according to Leake *et al.*, 1997), which is an unusual composition for mantle-derived amphibole. Type III-b samples contain less silicic edenite–Mg-katophorite (Fig. 8a). Cr contents (Fig. 8b) are high only in amphiboles related to metasomatic replacement of spl-I. Fluorine and Cl were not detected by electron microprobe. Trace element patterns show enrichment in U and Th, strongly negative Hf and Zr anomalies, and enrichment of LREE over HREE (Fig. 9a and b). Amphibole from sample Ke 1965/15 has the lowest HREE concentrations, but in contrast, exhibits a conspicuous positive Ti anomaly (Fig. 9b). Nb and Ta contents vary considerably, with the highest abundances in euhedral Mg-katophorite (Table 4; Fig. 9c). Compared with typical mantle amphiboles (e.g. Ionov *et al.*, 1997) the Mg-katophorites show a large compositional range (e.g. Fig. 10a). They are, however, remarkably depleted in large ion lithophile elements (LILE; e.g. 1·26–83 μg/g Ba compared with 75–1400 μg/g as reported for mantle amphibole from several off-craton xenolith suites; see Ionov *et al.*, 1997), and show low LILE/LREE ratios (Fig. 10b).

Phlogopite

Phlogopites (Table 5) have very high Na_2O contents (up to 2·88 wt%). Ti concentrations are mostly very low, and Mg-numbers are high (>93). Fluorine and Cl were not detected by electron microprobe. Generally, Na-rich phlogopites have higher U and Th concentrations and lower HFSE contents than phlogopite from the Group I (grt)–spl lherzolites (Kaeser *et al.*, 2006; Fig. 9a). Some trace elements show very broad ranges between samples (e.g. Nb ranging from 1·02 μg/g in Ke 785* to 47·9 μg/g in Ke 1965/3).

Apatite

Considerable differences were found between the two textural types of apatite (early in sample Ke 1965/3 and phosphate globules associated with glass in Ke 1959/15). Microprobe analyses only poorly satisfy apatite stoichiometry and show fairly low totals (Table 5). This is probably due to the abundant inclusions, which are inevitably included in the analysis. Early apatite is F-rich (1·89–2·53 wt% F) with variable Cl contents (0·92–1·57 wt%). It has extremely high REE and SrO contents (3·38–5·24 wt%; see Table 5). The MgO, Na_2O and FeO_{tot} contents are typical for upper mantle apatites (O'Reilly & Griffin, 2000).

In contrast, apatite globules in silicate glass are Cl-rich (2·96–3·14 wt% Cl) and have lower SrO and Na_2O, but slightly higher FeO_{tot} contents (Table 5). Both types of apatite are strongly LREE enriched [$(La/Yb)_N$ up to 783] and are the major host for U and Th (up to 33 500 times primitive mantle values), whereas HFSE concentrations are very low (Fig. 11b).

Late (glass-bearing) assemblages

Silicate glass

Representative results of microprobe and LA-ICPMS analyses of silicate glass are given in Table 6 and selected compositional plots are displayed in Fig. 12a–f. Generally, glass is siliceous (up to 66 wt% SiO_2) and peraluminous (12·45–25·07 wt% Al_2O_3) with characteristics (very low MgO and FeO, high alkalis) similar to those in many other xenolith suites (e.g. Ionov *et al.*, 1994; Zinngrebe & Foley, 1995; Chazot *et al.*, 1996*a*; Neumann & Wulff-Pedersen, 1997; Draper & Green, 1997; Varela *et al.*, 1999; Coltorti *et al.*, 2000; Laurora *et al.*, 2001; Shaw & Klügel, 2002; Ban *et al.*, 2005). Mg-numbers are commonly high (up to ~70; Fig. 12b). Considerable compositional heterogeneity can occur on a very small scale within individual samples. In sample 785*, for examples, glass in the vicinity of Opx_m contains up to 65 wt% SiO_2, whereas a nearby melt pocket (at less than 5 mm distance) contains glass with ~58 wt% SiO_2.

With respect to trace elements, glass is always LREE enriched [$(La/Yb)_N$ up to 77] at variable absolute REE concentrations (Fig. 13; Yb_N from 1·4 to 91·0). Zr, Hf and

Table 2: Representative analyses of clinopyroxene (oxides in wt%; trace elements in μg/g)

Type:	III-a			III-b			III-c				III-d
Mineral:	cpx-I	cpx-I	cpx-I	cpx-I	cpx-I	Di_m	Di_m	Di_m	Di_m	Ti-aug.	cpx
Sample:	1965/1	1965/1	1965/1	1965/15	1959/15	1959/15	1965/3	785*	1959/27	1959/27	1970/6
Texture:	Zone A[1]	Zone B[1]	Zone C[1]	core	core	core	micro-xx	micro-xx	micro-xx	micro-xx	core
	core	rim	core		high-Na		core	core	core	rim	high-Na
SiO_2	52·46	53·22	53·25	53·10	54·10	51·89	54·33	53·88	54·29	47·57	53·90
TiO_2	0·15	0·16	0·14	0·40	0·20	0·22	0·12	0·37	0·16	2·71	0·07
Al_2O_3	3·51	3·56	3·96	4·36	4·25	4·09	1·99	2·19	2·75	6·92	3·89
Cr_2O_3	1·35	1·21	1·12	1·39	1·37	2·03	5·45	3·62	2·24	1·46	2·84
$FeO_{(tot)}$	2·28	1·79	1·74	1·96	2·10	2·04	1·83	2·06	2·44	3·34	2·53
MnO	0·04	0·06	0·02	0·04	0·07	0·04	0·09	0·07	0·14	0·13	0·04
NiO	0·09	n.a.	n.a.	0·05	0·03	0·02	0·04	0·03	n.d.	0·05	n.d.
MgO	16·11	16·32	16·09	15·94	15·66	16·53	15·85	16·67	16·96	14·39	16·04
CaO	21·98	22·22	21·71	20·30	19·81	22·64	17·38	19·70	19·81	21·95	18·41
Na_2O	1·27	1·34	1·51	1·93	2·41	0·63	2·92	1·67	1·72	0·80	2·32
K_2O	n.d.	n.d.	n.d.	0·03	0·01	0·01	0·01	n.d.	n.d.	0·04	n.d.
Total	99·26	99·88	99·54	99·50	100·00	99·49	100·01	100·24	100·51	99·34	100·02
Mg-no.	92·66	94·19	94·27	93·55	93·02	93·53	93·92	93·52	92·54	88·48	91·89
P	12·6	16·9	16·8	21·6	65·5	61·1	113·5	46·8	61·1	78·6	129
K	6·64	0·86	9·85	198	18·6	<8·39	13·7	112	187	76·6	11·4
Sc	41·6	64·6	46·4	24·3	69·2	119	97·0	108	73·6	60·4	78·6
Ti	747	816	828	2027	1053	875	613	1663	1022	9622	439
V	233	245	249	275	278	261	378	525	234	385	303
Ni	287	269	277	302	294	348	368	411	316	472	329
Zn	5·85	5·87	6·79	9·14	13·7	4·40	7·93	10·8	15·0	29·3	10·9
Ga	2·32	1·68	2·39	4·73	n.a.	n.a.	n.a.	4·40	n.a.	n.a.	3·58
Rb	0·015	0·013	0·016	0·16	<0·076	<0·21	0·051	0·13	0·49	0·33	<0·008
Sr	52·8	58·0	118	98·6	106	47·4	687	47·0	218	115	484
Y	3·62	10·6	2·32	1·65	11·0	18·1	73·9	19·9	40·6	22·9	43·6
Zr	8·35	10·0	7·90	10·4	13·0	4·792	22·6	2·29	53·5	53·6	17·4
Nb	0·13	0·051	0·045	0·14	0·14	0·28	3·58	0·070	1·13	0·72	1·16
Cs	0·003	<0·002	<0·002	0·005	<0·032	<0·069	<0·019	<0·020	<0·018	<0·079	<0·002
Ba	0·60	0·047	4·23	4·44	0·28	<0·63	0·47	0·38	6·02	<0·79	0·085
La	0·97	3·04	6·81	2·59	13·9	12·2	88·4	2·80	8·82	3·95	21·7
Ce	2·43	5·03	7·05	5·48	21·6	37·7	195	13·7	37·1	14·6	90·3
Pr	0·45	0·53	0·56	0·73	1·66	4·78	23·9	2·64	6·93	2·68	16·1
Nd	2·39	2·42	2·38	3·57	5·38	19·6	99·5	13·3	38·5	16·7	86·4
Sm	0·78	0·88	0·71	1·17	1·10	2·41	18·4	3·9	12·9	5·94	21·4
Eu	0·35	0·37	0·28	0·43	0·37	1·22	6·21	1·36	4·00	2·25	7·41
Gd	0·85	1·10	0·79	0·87	1·10	3·11	14·3	3·87	12·2	4·11	16·4
Tb	0·13	0·24	0·11	0·10	n.a.	n.a.	n.a.	0·68	n.a.	n.a.	2·33
Dy	0·72	1·72	0·55	0·49	1·64	2·35	13·4	4·96	9·23	5·03	11·2
Ho	0·13	0·38	0·094	0·068	0·37	0·79	2·58	0·81	1·66	0·84	1·82
Er	0·35	1·18	0·17	0·15	1·17	1·24	7·07	2·09	4·15	1·86	3·79
Tm	0·056	0·19	0·027	0·017	0·16	0·24	0·95	0·22	0·53	0·24	0·39
Yb	0·51	1·28	0·16	0·12	0·95	1·92	5·67	1·37	3·36	2·80	2·11
Lu	0·087	0·18	0·022	0·015	0·22	0·28	0·70	0·089	0·42	0·15	0·24

(continued)

Table 2: Continued

Type:	III-a			III-b			III-c				III-d
Mineral:	cpx-I	cpx-I	cpx-I	cpx-I	cpx-I	Di_m	Di_m	Di_m	Di_m	Ti-aug.	cpx
Sample:	1965/1	1965/1	1965/1	1965/15	1959/15	1959/15	1965/3	785*	1959/27	1959/27	1970/6
Texture:	Zone A[1]	Zone B[1]	Zone C[1]	core	core	core	micro-xx	micro-xx	micro-xx	micro-xx	core
	core	rim	core		high-Na		core	core	core	rim	high-Na
Hf	0·34	0·31	0·28	0·50	0·25	0·40	0·81	0·056	1·02	2·42	0·23
Ta	0·011	0·007	0·016	0·021	<0·029	<0·080	0·657	<0·012	0·043	<0·19	0·056
Pb	0·37	0·50	0·58	1·15	0·68	<0·35	0·23	<0·28	<0·089	<0·39	0·11
Th	0·12	0·41	1·31	0·73	4·94	0·38	0·45	0·019	0·062	<0·074	0·062
U	0·076	0·27	0·47	0·28	1·29	<0·078	0·049	<0·018	0·030	<0·071	0·017

[1]See Fig. 15.
n.d., not detected; n.a., not analysed.

Ti are depleted relative to the REE, and Nb and Ta relative to U and Th. Trace element compositions always mirror the composition of the associated earlier phases (i.e. amphibole in most cases but also clinopyroxene, orthopyroxene, phlogopite and apatite).

Glass in Group III xenoliths is clearly different compared with Ti-rich subalkaline glass occasionally found in Group I lherzolites from Marsabit (related to melting of Ti-pargasite; see Kaeser, 2006, and Fig. 12a–f). Also, glass is generally clearly distinct from the xenolith-hosting basanites (Fig. 12a–f). The exception is glass within the Type III-c dunite Ke 1959/27 and from the margin of xenolith Ke 1965/15 (contact with host lava), which show some important differences compared with glass from the other samples; that is, higher FeO and lower SiO_2 contents, similar to the composition of the host basanite (Figs 12a–f and 13).

Clinopyroxene micro-phenocrysts

Clinopyroxene micro-phenocrysts (Di_m) are Na-rich Cr diopsides (up to 3·23 wt% Na_2O and 6·45 wt% Cr_2O_3; Fig. 6a and b) with low TiO_2 contents (<0·5 wt%) and high Mg-numbers (up to 94·9). In all samples, Di_m are strongly zoned with Cr and Na contents generally decreasing from cores to rims (Fig. 6b). Di_m in contact with basanitic glass in the kaersutite-bearing dunite (Ke 1959/27) has resorbed rims, overgrown by Ti-augite (Fig. 4f) with significantly lower Na_2O (<1 wt%) contents and Mg-numbers (≥85; see Table 2).

Trace element patterns of Di_m are similar in shape to the associated glass (except LILE: Cs to U; Fig. 13). Negative HFSE anomalies are mostly due to higher REE abundances; that is, the absolute concentrations of HFSE are similar to those of cpx-I from Type III-a and -b (see Fig. 7a; no real HFSE depletion). Texturally equilibrated clinopyroxene in the Type III-d spl harzburgite (Ke 1970/6; Fig. 3f) is a Na-rich Cr diopside with similar major (Fig. 6a) and trace element characteristics (Fig. 7b) similar to those of the glass-hosted micro-phenocryst cores.

Olivine, spinel, kaersutite

Compared with ol-I, glass-related Ol_m is more magnesian (Table 3; up to $Fo_{94.6}$) and enriched in Ca. Ol-I in contact with glass develops strong compositional gradients approaching the composition of Ol_m at the rims. Spinel micro-phenocrysts (Chr_m) are Mg-rich chromites (Cr-number up to 66·5), enriched in (calculated) Fe_2O_3 compared with spl-I.

Kaersutite occurs as tiny rims on amphibole in Type III-b and -c, and as micro-phenocrysts in Type III-c sample Ke 1959/27. Reaction rims are characterized by higher Mg-numbers than the original amphibole. They are too narrow to be analysed for trace elements. Kaersutite micro-phenocrysts in sample Ke 1959/27 have low Mg-number (about 82) and high K_2O contents (Table 4). Major element characteristics as well as trace element patterns (convex-upward REE patterns, high Nb–Ta, low U–Th; Fig. 9d) are similar to those of hornblendites and amphibole megacrysts from alkaline magmas (e.g. Shaw & Eyzaguirre, 2000).

Carbonates

Most glass-related carbonate globules contain Mg-calcite (Table 7) with an average Mg-number of 96·5 and Ca/(Ca + Mg) between 0·87 and 0·98. In sample Ke 1965/3, MgO correlates positively with SrO (up to 5·35 wt% MgO and 0·89 wt% SrO). Other elements show very low concentrations (Table 7). One sample (Type III-c Ke 1959/15) contains zoned crystals ranging from dolomitic to calcitic in composition (Fig. 5a). Carbonates have low REE contents with flat to slightly LREE-enriched

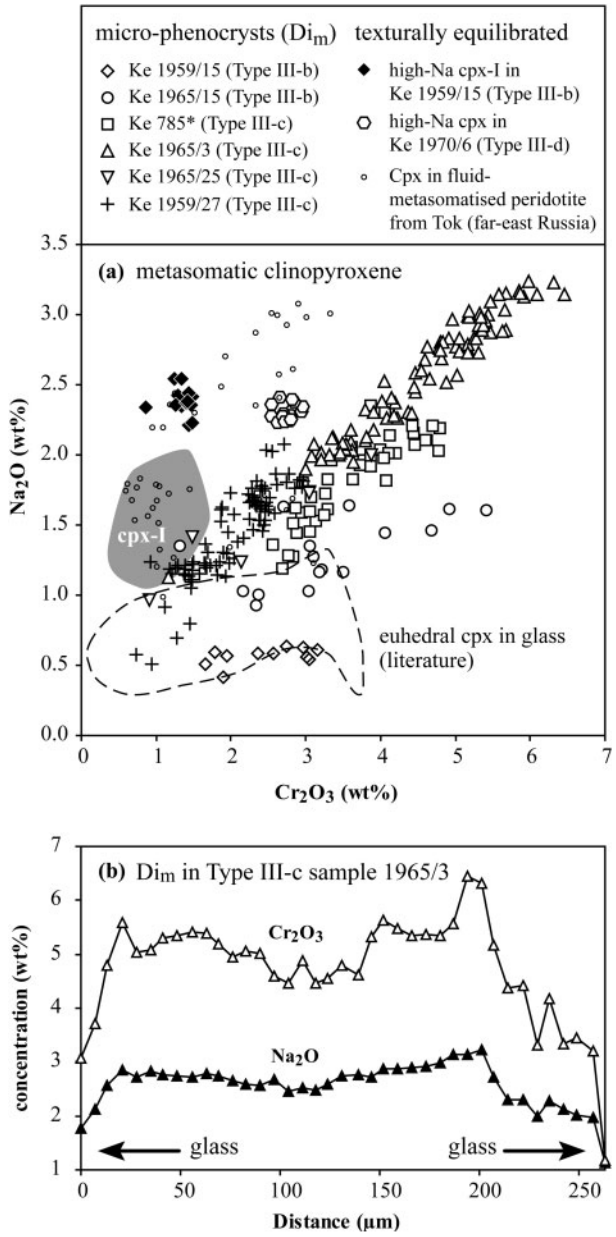

Fig. 6. Major element composition of clinopyroxene in porphyroclastic spinel harzburgite and dunite xenoliths from Marsabit. (a) Plot of Cr_2O_3 *vs* Na_2O (wt%) in micro-phenocrysts compared with cryptically metasomatized cpx-I in Type III-b sample Ke 1959/15, texturally equilibrated Na-rich clinopyroxene in Type III-d sample Ke 1970/6 and texturally equilibrated Na-rich cpx from fluid-metasomatized peridotite from Tok (far-east Russia; Ionov *et al.*, 2005). The dashed line outlines the compositional range of common low-Na micro-phenocrysts in glass from other xenolith suites (see Ionov *et al.*, 2005, and references therein). Crosses show the compositional variation of micro-phenocrysts in the Group III-c xenolith 1959/27 (i.e. Di_m overgrown by low-Na and low-Cr Ti-augite; see Fig. 4f). Compositional range of primary cpx-I in all Group III xenoliths (cpx-I; grey field) is from Kaeser *et al.* (2006). (b) Na_2O and Cr_2O_3 (wt%) variation across a single Di_m micro-phenocryst in Type III-c xenolith Ke 1965/3 (electron microprobe profile).

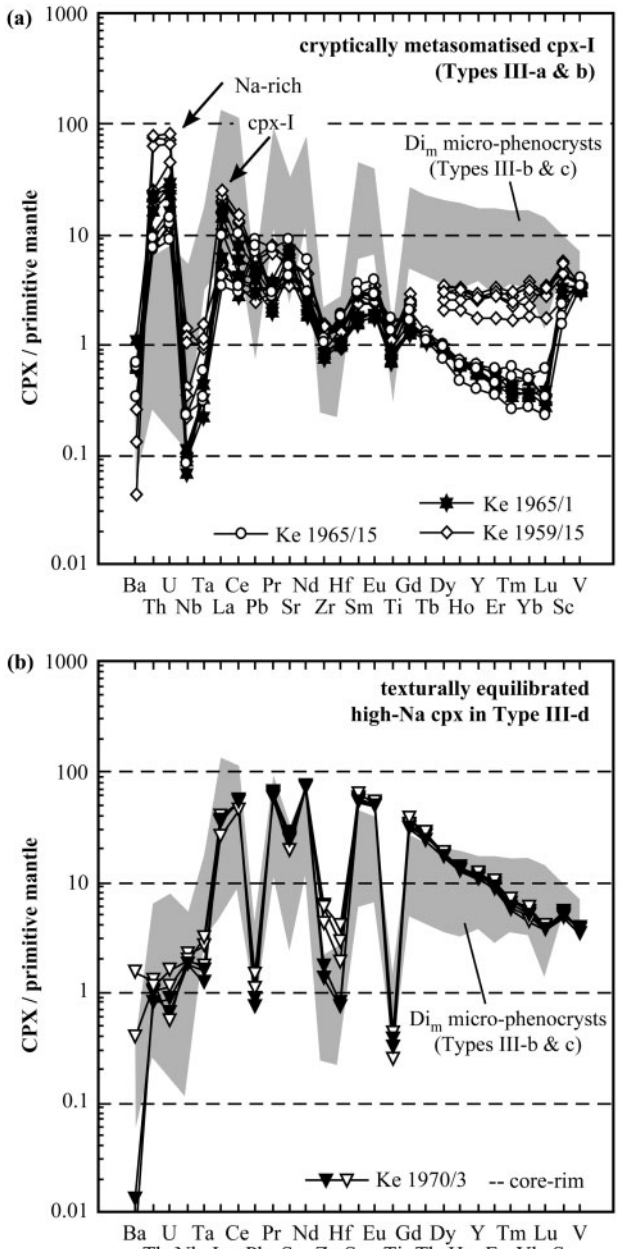

Fig. 7. Trace element composition of clinopyroxene from the porphyroclastic spinel harzburgites from Marsabit [normalized to the primitive mantle values of McDonough & Sun (1995)]. (a) Trace element patterns of primary cryptically metasomatized clinopyroxene (cpx-I) in Type III-a and -b spinel harzburgites. Small arrows indicate high-Na cpx-I in Type III-b sample Ke 1959/15 (see also Fig. 6a). (b) Trace element patterns of texturally equilibrated Na-rich Cr diopside from the recrystallized Type III-d spinel harzburgite. The shaded fields indicate the compositional range of glass-related clinopyroxene microphenocrst (Di_m).

patterns (Fig. 14). Extended trace element plots exhibit a very broad range of concentrations in different samples (e.g. Pb; Fig. 14). Large positive peaks for U, Pb and Sr are typical. In addition, U and Nb are strongly enriched

Table 3: Representative analyses of orthopyroxene, spinel and olivine (oxides in wt%; trace elements in μg/g)

Type:	III-a	III-b	III-b	III-c	III-d	III-c	III-d	III-c	III-c	III-c	III-d
Mineral:	opx-I	opx-I	opx-I	Opx_m	Opx_m	Chr_m	spl-I	ol-I	Ol_m	ol-I	ol-I
Sample:	1965/1	1965/15	1959/15	1965/3	1970/6	1965/3	1970/6	785*	1965/3	1965/25	1970/6
Texture:	Zone C[1] core	core	core	core	core	core	core	core	core	core	core
SiO_2	56·57	56·42	56·15	58·07	57·13	0·12	0·05	40·93	41·35	40·78	40·98
TiO_2	0·04	0·13	0·06	0·01	0·05	0·44	0·16	n.d.	0·01	0·01	n.d.
Al_2O_3	2·65	2·69	2·99	0·46	1·92	12·23	18·80	0·01	0·01	n.d.	0·04
Cr_2O_3	0·43	0·56	0·40	0·32	0·54	54·54	50·43	0·01	0·29	0·01	0·05
Fe_2O_3	—	—	—	—	—	5·54	3·38	—	—	—	—
$FeO_{(tot)}$	5·33	5·68	5·76	5·38	4·86	11·14	12·07	9·39	5·83	11·33	7·71
MnO	0·13	0·14	0·14	0·12	0·12	n.a.	0·05	0·15	0·13	0·27	0·07
NiO	n.a.	0·10	0·09	0·07	0·09	0·15	0·09	0·40	0·24	0·37	0·39
MgO	34·73	34·20	33·80	35·61	34·64	14·80	15·02	49·00	51·82	47·39	50·13
CaO	0·51	0·53	0·48	0·20	0·52	0·03	0·00	0·01	0·08	0·02	0·08
Na_2O	0·05	0·08	0·13	0·09	0·14	n.a.	n.a.	0·01	0·04	n.d.	0·01
Total	100·44	100·52	100·00	100·34	100·02	99·10	100·08	99·92	99·80	100·18	99·47
Mg-no.	92·08	91·48	91·28	92·18	92·71	70·32	68·94	90·29	94·06	88·17	92·06
Na	341	423	1136	539	1120	n.a.	4·38	29·7	262	64·7	230
Al	15120	14586	17785	1817	10834	n.a.	114911	8·93	82·1	12·0	1201
P	15·6	14·5	17·5	17·5	24·8	n.a.	19·8	42·1	292	105	244
Ca	3163	3016	3881	1487	3895	n.a.	<53·48	82·2	579	200	658
K	1·72	<0·44	<0·35	98·1	1·50	n.a.	<0·86	<0·37	<1·02	1·98	6·30
Sc	8·05	5·46	17·3	2·44	12·4	n.a.	2·80	0·61	4·32	0·94	2·86
Ti	239	619	366	44·9	227	n.a.	956	1·56	8·71	1·70	20·4
V	76·8	90·6	77·2	14·9	63·4	n.a.	925	1·04	3·77	0·96	28·3
Ni	568	646	585	588	748	n.a.	1010	2686	2875	2920	2649
Zn	25·6	30·1	24·5	60·6	37·3	n.a.	732	63·0	66·5	146	69·3
Ga	1·81	3·50	n.a.	n.a.	1·33	n.a.	28·0	0·015	n.a.	0·035	0·77
Sr	0·24	0·14	0·44	1·02	1·67	n.a.	0·089	0·017	<0·013	0·045	0·52
Y	0·081	0·073	0·49	0·69	2·02	n.a.	0·025	0·015	0·16	0·10	0·19
Zr	0·23	0·277	0·51	0·038	0·88	n.a.	1·24	<0·005	<0·033	<0·006	0·15
Nb	<0·005	0·020	<0·007	0·18	0·051	n.a.	0·877	<0·003	0·025	0·008	0·035
Ba	0·056	<0·018	<0·021	7·48	0·035	n.a.	<0·028	<0·016	<0·071	0·17	0·13
La	0·019	<0·002	0·055	0·061	0·045	n.a.	0·039	0·021	<0·004	0·017	0·019
Ce	0·020	0·005	0·046	0·109	0·27	n.a.	0·052	0·023	<0·012	0·027	0·15
Pr	0·002	<0·001	0·005	0·007	0·064	n.a.	0·024	<0·001	<0·011	0·009	0·019
Nd	<0·008	0·010	0·043	0·039	0·42	n.a.	<0·029	<0·007	<0·052	0·018	0·11
Sm	0·014	<0·009	0·016	<0·018	0·19	n.a.	0·022	<0·006	<0·051	<0·009	0·032
Eu	<0·003	<0·002	<0·005	0·012	0·077	n.a.	0·018	<0·002	<0·012	<0·003	0·011
Gd	<0·014	<0·006	0·028	0·021	0·20	n.a.	<0·026	<0·006	<0·041	<0·016	0·035
Tb	0·002	<0·001	n.a.	n.a.	0·045	n.a.	<0·004	<0·001	n.a.	<0·001	0·004
Dy	0·015	0·011	0·086	0·058	0·38	n.a.	0·010	<0·003	<0·043	<0·009	0·041
Ho	0·007	0·003	0·012	0·031	0·069	n.a.	0·003	<0·001	<0·006	0·004	0·010
Er	<0·012	0·008	0·043	0·094	0·22	n.a.	<0·015	<0·006	0·058	0·018	0·027
Tm	0·002	0·001	0·015	0·014	0·031	n.a.	<0·003	<0·001	0·010	0·003	0·004
Yb	0·027	0·011	0·19	0·170	0·28	n.a.	<0·018	0·009	0·064	0·060	0·038
Lu	0·001	0·002	0·026	0·026	0·033	n.a.	0·007	0·002	0·040	0·018	0·008

(continued)

Table 3: Continued

Type:	III-a	III-b	III-b	III-c	III-d	III-c	III-d	III-c	III-c	III-c	III-d
Mineral:	opx-I	opx-I	opx-I	Opx_m	Opx_m	Chr_m	spl-I	ol-I	Ol_m	ol-I	ol-I
Sample:	1965/1	1965/15	1959/15	1965/3	1970/6	1965/3	1970/6	785*	1965/3	1965/25	1970/6
Texture:	Zone C[1] core	core	core	core	core	core	core	core	core	core	core
Hf	0·006	0·010	0·014	<0·009	0·013	n.a.	0·042	<0·003	<0·017	<0·009	<0·006
Ta	<0·001	<0·001	<0·004	<0·005	<0·002	n.a.	0·015	0·001	<0·018	<0·001	<0·001
Pb	<0·028	0·041	0·047	0·074	<0·041	n.a.	0·15	0·036	0·075	0·042	0·046
Th	0·009	<0·002	0·069	0·020	<0·002	n.a.	0·010	0·050	<0·006	0·011	<0·001
U	0·004	<0·001	0·026	0·017	0·004	n.a.	0·017	0·011	<0·006	<0·001	<0·002

[1]See Fig. 15.
n.d., not detected; n.a., not analysed.

Table 4: Representative analyses of amphibole (oxides in wt%; trace elements in μg/g)

Type:	III-b				III-c					
Mineral:	katoph.	katoph.	katoph.	katoph.	katoph.	katoph.	katoph.	katoph.	kaersut.	kaersut.
Sample:	1959/15	1965/15	1965/15	1965/15	785*	785*	1965/25	1965/25	1959/27	1959/27
Texture:	residual in m.p.	interst.	interst.	lamellae in cpx-I	residual in m.p.	residual in m.p.	euhedral core	euhedral rim	micro-xx	micro-xx
SiO_2	45·41	46·03	46·25	48·87	49·55	49·59	49·52	49·53	40·64	41·06
TiO_2	0·15	1·90	2·03	0·99	0·30	0·29	0·22	0·28	6·12	5·77
Al_2O_3	13·65	11·45	11·00	9·15	8·26	8·07	8·77	7·94	14·05	13·95
Cr_2O_3	2·51	1·23	1·48	1·44	2·54	2·63	1·06	1·15	0·31	0·08
$FeO_{(tot)}$	3·50	2·93	3·04	2·78	3·02	2·94	3·59	3·46	5·88	6·15
MnO	0·06	0·03	0·04	0·02	0·08	0·02	0·10	0·08	0·16	0·10
NiO	0·09	0·14	0·09	0·10	0·10	0·06	0·09	0·12	0·10	0·10
MgO	18·83	18·86	18·96	19·97	20·67	20·62	20·00	20·24	15·76	15·45
CaO	8·51	9·74	9·60	9·76	8·05	7·93	8·63	9·09	10·86	10·75
Na_2O	4·74	4·27	4·40	4·32	5·48	5·55	5·29	5·09	2·84	2·94
K_2O	0·49	0·38	0·41	0·31	0·27	0·29	0·28	0·39	1·39	1·38
Total	98·11	96·95	97·28	97·71	98·37	98·05	97·59	97·41	98·17	97·93
Mg-no.	90·55	91·99	91·76	92·75	92·43	92·59	90·86	91·24	82·69	81·73
P	445	222	235	n.a.	175	196	206	120	214	266
K	4301	3916	3637	n.a.	2393	2654	2955	3655	13289	12762
Sc	40·2	7·04	6·63	n.a.	35·8	34·5	31·1	35·2	37·5	27·0
Ti	720	9867	9917	n.a.	1732	1898	1421	1589	32154	32071
V	216	317	332	n.a.	289	299	172	187	469	404
Ni	726	842	828	n.a.	811	876	737	813	638	530
Zn	29·8	16·3	15·9	n.a.	18·8	21·4	45·1	45·7	46·3	54·8
Ga	n.a.	9·81	9·39	n.a.	10·3	11·4	8·67	8·72	n.a.	n.a.
Rb	2·79	1·84	1·51	n.a.	0·35	0·50	0·96	1·50	7·44	7·13
Sr	216	325	335	n.a.	70·8	66·7	95·5	117	618	668
Y	10·1	2·69	3·15	n.a.	11·1	12·6	39·0	35·9	31·0	35·5
Zr	5·39	3·70	3·31	n.a.	2·92	2·97	11·4	59·2	93·3	110
Nb	3·39	4·13	4·47	n.a.	1·02	1·21	19·2	70·5	26·5	34·1
Cs	0·006	<0·001	0·005	n.a.	0·006	<0·009	0·008	0·018	<0·019	<0·010

(continued)

Table 4: Continued

Type:	III-b				III-c					
Mineral:	katoph.	katoph.	katoph.	katoph.	katoph.	katoph.	katoph.	katoph.	kaersut.	kaersut.
Sample:	1959/15	1965/15	1965/15	1965/15	785*	785*	1965/25	1965/25	1959/27	1959/27
Texture:	residual in m.p.	interst.	interst.	lamellae in cpx-I	residual in m.p.	residual in m.p.	euhedral core	euhedral rim	micro-xx	micro-xx
Ba	78·1	61·4	54·0	n.a.	2·59	3·09	8·46	8·41	331	322
La	35·7	11·6	11·0	n.a.	7·04	8·24	17·7	11·3	10·7	13·8
Ce	62·7	22·5	23·1	n.a.	21·7	24·8	62·1	42·6	33·8	44·8
Pr	5·74	2·08	2·24	n.a.	3·01	3·49	8·56	6·23	5·57	7·24
Nd	17·7	7·20	7·79	n.a.	12·8	15·1	36·3	29·6	31·8	39·8
Sm	2·08	1·43	1·43	n.a.	2·85	3·16	7·52	7·40	9·45	11·1
Eu	0·80	0·58	0·60	n.a.	1·08	1·15	2·32	2·52	3·63	3·84
Gd	1·82	0·85	0·88	n.a.	2·25	2·41	7·01	6·92	9·40	9·80
Tb		0·11	0·13	n.a.	0·39	0·50	1·20	1·17	n.a.	n.a.
Dy	1·71	0·57	0·67	n.a.	2·02	2·52	7·35	6·98	7·00	8·19
Ho	0·36	0·10	0·10	n.a.	0·39	0·50	1·55	1·44	1·37	1·47
Er	1·06	0·24	0·27	n.a.	0·97	1·14	4·05	3·82	2·96	3·36
Tm	0·16	0·030	0·033	n.a.	0·12	0·17	0·60	0·58	0·27	0·39
Yb	1·20	0·28	0·30	n.a.	0·77	0·99	4·00	3·86	2·43	2·72
Lu	0·19	0·036	0·038	n.a.	0·079	0·077	0·58	0·44	0·33	0·31
Hf	0·15	0·067	0·054	n.a.	0·065	0·048	0·28	0·78	3·31	3·76
Ta	0·033	0·14	0·14	n.a.	0·002	0·004	0·10	1·07	1·67	1·98
Pb	2·01	3·60	3·74	n.a.	1·42	1·73	1·95	2·22	0·22	0·39
Th	6·82	1·50	1·34	n.a.	1·81	1·96	0·59	0·28	0·10	0·20
U	2·12	0·39	0·39	n.a.	0·40	0·48	0·19	0·12	0·018	0·048

katoph., Mg-katophorite; kaersut., kaersutite; interst., interstitial; m.p., melt pocket; n.d., not detected; n.a., not analysed.

compared with Th and Ta, respectively. Hf, Zr and Ti show very low concentrations. Overall, major and trace element characteristics of the carbonates are similar to those of carbonates found in other peridotite xenoliths (e.g. Ionov, 1998; Lee *et al.*, 2000; Laurora *et al.*, 2001; Ionov & Harmer, 2002; see Fig. 14).

FORMATION OF THE EARLY ASSEMBLAGES

Despite large compositional variations, numerous common textural and compositional features indicate that the early metasomatic assemblages in all Group III samples formed during a single metasomatic event. In the discussion below, we argue that during a first metasomatic stage, the primary (pre-metasomatic) phase assemblage in Group III spinel harzburgites was partially replaced by metasomatic minerals, finally resulting in clinopyroxene-free amphibole- and phlogopite-bearing dunite and harzburgite (Type III-c). The initial metasomatic agent was probably an evolved CO_2–H_2O-rich melt, and the transition from peridotites of Type III-a to -c can be explained by progressive melt–rock reaction.

Transition from cryptic (Type III-a) to modal (Type III-b and -c) metasomatism

Formation of new phases requires (1) crystallization from a melt or fluid phase (decreasing melt or fluid mass) and/or (2) melt–solid or fluid–solid reaction. Textural features such as spinel being replaced by amphibole and phlogopite (e.g. Fig. 3c) indicate melt(fluid)–rock reaction. The geochemical signatures observed in the different peridotite types thus probably reflect pre-existing compositional heterogeneities coupled with metasomatic modification. This is illustrated best in sample Ke 1965/1 (Type III-a), the least metasomatized xenolith in this study. It can be subdivided into three parts containing clinopyroxene with different REE signatures (Zones A, B and C in Fig. 15). The LREE are increasingly enriched from Zone A to C, indicating increasing cryptic metasomatism.

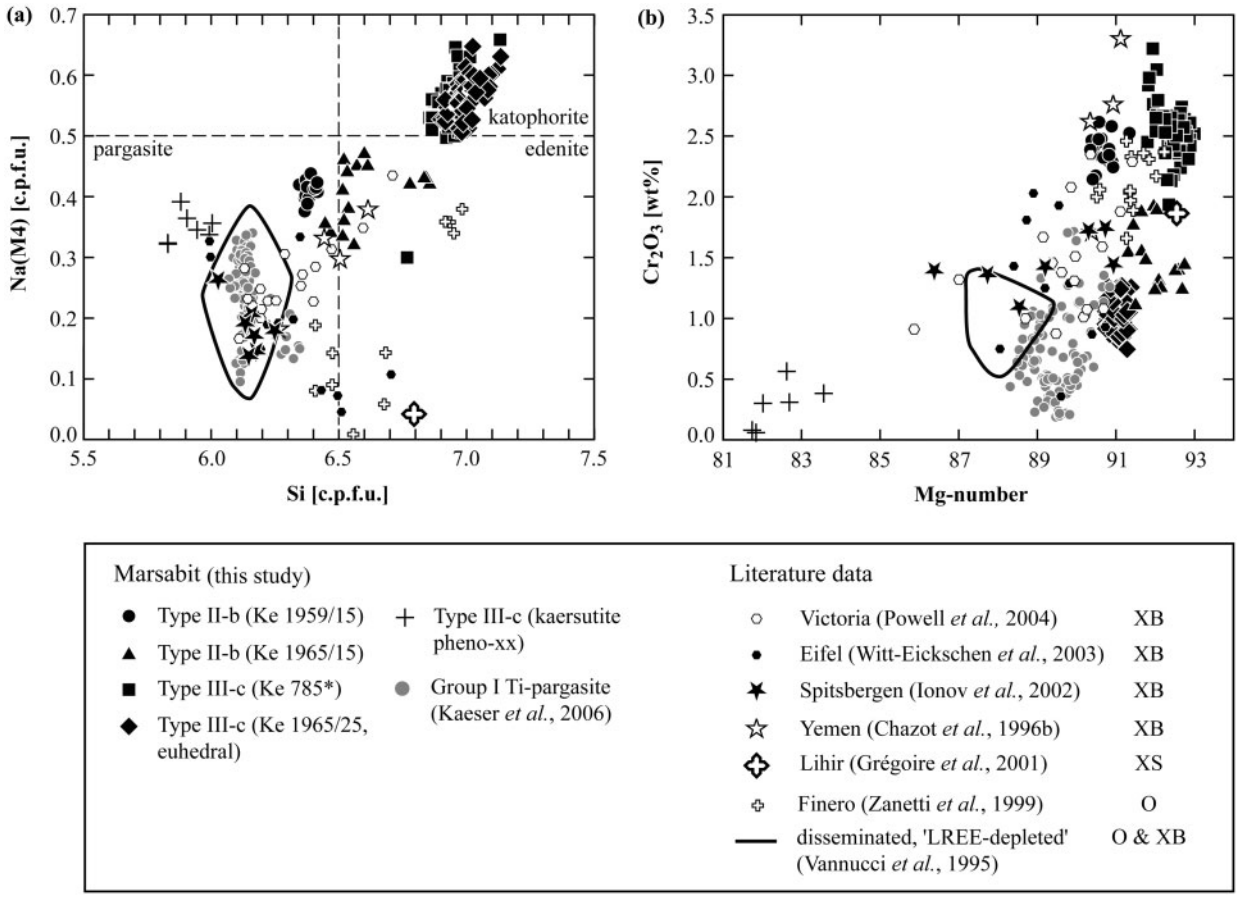

Fig. 8. Major element characteristics of amphiboles from porphyroclastic spinel harzburgites and dunites from Marsabit, compared with compositions of mantle-derived amphiboles from other localities (XB, basalt-hosted xenoliths; XS, xenoliths from subduction settings; O, orogenic peridotites). Mg-number = $Mg/(Mg + Fe_{tot})$ in molar proportions.

HREE abundances, on the other hand, are very heterogeneous in the least metasomatized Zone A, moderately depleted in Zone B, and homogeneously low in the most metasomatized Zone C (containing graphite; Fig. 15), similar to REE patterns in clinopyroxene from the amphibole- and phlogopite-bearing Type III-b sample (Ke 1965/15; Fig. 7a).

The decoupling of strongly (LREE, Th, U) from moderately incompatible elements (HREE) can be explained by chromatographic fractionation during percolation of small amounts of melts or fluids through an initially non-metasomatized peridotite (Navon & Stolper, 1987; Godard *et al.*, 1995; Bedini *et al.*, 1997; Vernières *et al.*, 1997; Ionov *et al.*, 2002). Upon reaction with the wall-rock, a fluid or melt will become progressively enriched in incompatible elements as a function of increasing distance from its source. This is due to the fact that elements with higher $D^{mineral/melt}$ values (e.g. HREE) are selectively removed from a percolating liquid when it exchanges with the surrounding minerals. The results are faster-moving chemical fronts of incompatible elements compared with those of more compatible elements. This is consistent with the geochemical signature of cpx-I from the least metasomatized part of sample Ke 1965/1 (Zone A; Fig. 15), which already started to re-equilibrate with respect to the incompatible elements (i.e. addition of Th, U and LREE) whereas more compatible elements still reflect pre-metasomatic heterogeneities. In this case, these are extreme HREE variations, probably reflecting the earlier garnet breakdown (Kaeser *et al.*, 2006). On the other hand, more intensely metasomatized parts (e.g. Zone C in sample Ke 1965/1 and sample Ke 1965/15) are characterized by clinopyroxene trace element patterns where mildly incompatible elements have also been modified (e.g homogeneously depleted HREE; Figs 7a and 15).

Similar fractionation processes can explain the modal and compositional differences between Type III-b and -c. Compared with Type III-b, higher abundances of metasomatic phases in Type III-c suggests that higher amounts of fluid or melt crystallized in, or passed through, these rocks. The amphibole-rich dunite (Ke 1965/25), for example, contains low-Ti Mg-katophorite exhibiting the lowest $(La/Yb)_N$ and $(La/Ce)_N$ ratios, and high $(Nb/La)_N$ and

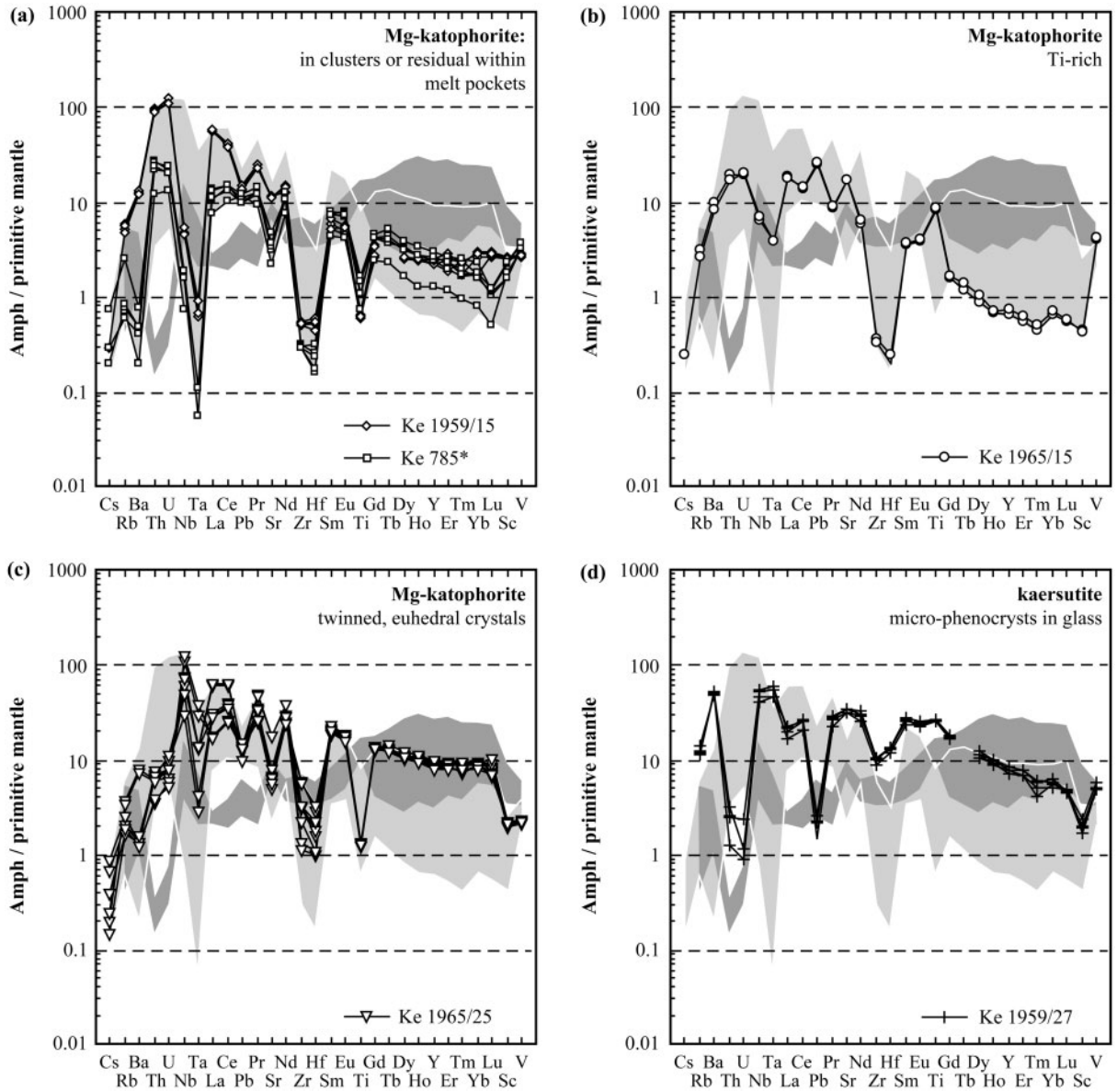

Fig. 9. Trace element composition of amphibole from porphyroclastic spinel harzburgites and dunites from Marsabit [normalized to the primitive mantle values of McDonough & Sun (1995)]: Mg-katophorite in Type III-b and -c xenoliths (a–c), and glass-related kaersutite (d). The shaded fields indicate the compositional variation of all Mg-katophorite analyses (light grey), and the compositional range of LREE-depleted Ti-pargasite from the Group I (grt)–spinel lherzolites (dark grey; Kaeser *et al.*, 2006).

$(Nb/Th)_N$ ratios (Fig. 10a and c), indicating a moderately fractionated metasomatic agent. Mg-katophorite from the phlogopite-rich harzburgite (Ke 785*; Type III-c), and amphiboles from the more cpx-rich harzburgites (Type III-b) show progressively more fractionated patterns (e.g. Fig. 10c) and decreasing abundances in 'amphibole-compatible' elements (e.g. Nb; Fig. 9a). Thus, the transition from Type III-b to -c could reflect decreasing distance between the site at which the xenolith was sampled and the source of the 'initial' metasomatizing agent (e.g. Zanetti *et al.*, 1996; Ionov *et al.*, 2002; Bodinier *et al.*, 2004). Judging from the abundance of modal metasomatic phases, the amphibole dunite (Ke 1965/25) was probably closest to the source of the metasomatizing agent. The phlogopite-rich nature of Ke 785*, which indicates higher K and LILE (Cs, Rb, Ba) contents in the remaining agent, is in agreement with a more fractionated melt or fluid, at somewhat greater distance from the metasomatic source.

The Nb abundances in amphibole also agree with this model as well. For example, amphibole from Type III-c Ke 1965/25 has comparatively high Nb concentrations (Fig. 9c), in line with relatively high $D_{Nb}^{amph/melt}$ values

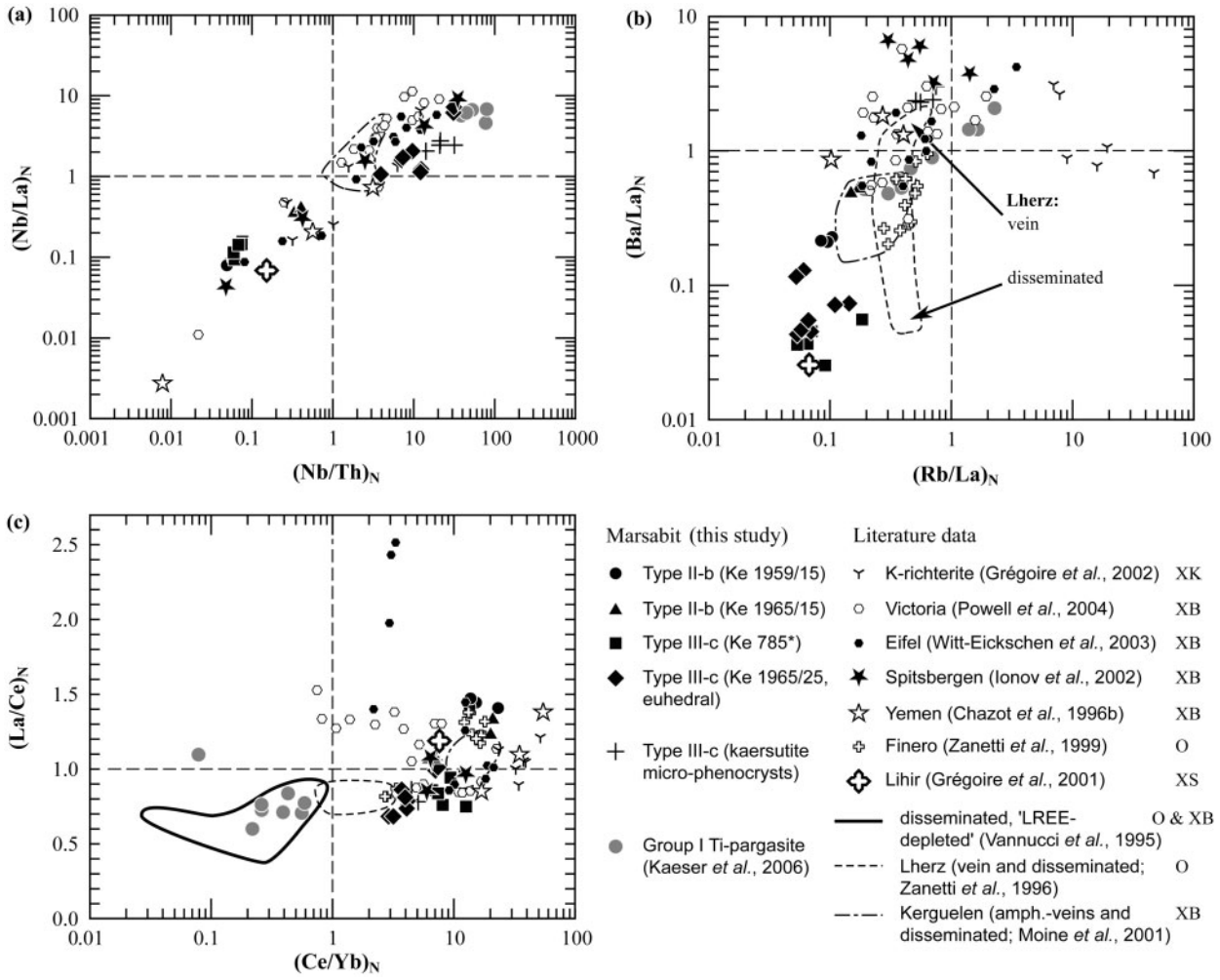

Fig. 10. Selected trace element ratios in amphiboles from the porphyroclastic spinel harzburgites from Marsabit compared with those of mantle-derived amphibole from other tectonic settings (XK and XB, cratonic, kimberlite-hosted and off-cratonic, basalt-hosted xenoliths, respectively; O, orogenic peridotites; XS, xenoliths from subduction settings). Concentrations (ratios) normalized to the primitive mantle values of McDonough & Sun (1995).

constrained by different studies (e.g. Ionov & Hofmann, 1995; LaTourrette *et al.*, 1995). In Ti-poor systems, such as those of this study, Nb uptake by amphibole is even enhanced as a result of increased D_{Nb} values (Tiepolo *et al.*, 2001). Consequently, in an event during which amphibole crystallizes continuously, the remaining fluid or melt will become progressively depleted in Nb (Ionov *et al.*, 2002), resulting in formation of Nb-depleted amphiboles further away from the source (Zanetti *et al.*, 1996; Ionov *et al.*, 2002); such Nb-depleted amphibole is found in sample Ke 785*, as well as in Type III-b xenoliths (e.g. Ke 1959/15; Fig. 9a). Amphibole signatures from xenolith suites modelled successfully in the context of percolative trace element fractionation (e.g. Spitsbergen; Ionov *et al.*, 2002) show similar ranges (e.g. in Nb/Th ratios; Fig. 10a) to those documented for our samples. This further supports the hypothesis that similar percolation mechanisms acted in the mantle beneath Marsabit.

The role of pre-existing heterogeneities and exotic minerals

Although a model based on trace element fractionation during melt percolation is supported by textures and can account for many compositional features, some compositional peculiarities remain unexplained. First, clinopyroxene and amphibole in several samples (Ke 785*, 1965/1 and 1965/15) are characterized by extremely low HREE abundances, more than one order of magnitude lower than in amphiboles from the strongly metasomatized amphibole dunite Ke 1965/25 (Fig. 9a–c). The main phases that crystallize during metasomatism are low-Ti Mg-katophorite and phlogopite. However, $D_{HREE}^{amph/melt}$

Table 5: Representative analyses of phlogopite and apatite (oxides in wt%; trace elements in μg/g)

Type:	III-b		III-c						III-b	III-c
Mineral:	phlog.	phlog.	phlog.	phlog.	phlog.	phlog.	phlog.		apatite	apatite
Sample:	1965/15	1965/15	1965/3	785	785	785	1965/25		1959/15	1965/3
Texture:	veinlet	interst.	in opx	in opx	with amph in m.p.	around chromite	incl. in amph		bleb in glass	interst. grain
SiO_2	39·25	39·14	41·71	41·90	41·24	41·34	42·30	SiO_2	0·16	0·49
TiO_2	3·13	3·07	0·09	0·53	0·39	0·37	0·27	Al_2O_3	0·01	n.d.
Al_2O_3	15·44	15·83	13·60	13·60	13·84	13·77	14·77	P_2O_5	37·68	37·15
Cr_2O_3	1·12	1·05	1·32	1·47	1·90	1·97	0·63	$FeO_{(tot)}$	0·37	0·29
$FeO_{(tot)}$	3·50	3·47	2·71	0·00	2·89	2·77	3·40	MnO	0·06	n.d.
MnO	n.d.	0·02	0·08	3·05	0·04	0·02	0·05	MgO	0·84	0·91
NiO	0·23	0·27	0·19	0·23	0·24	0·28	0·23	CaO	47·50	42·37
MgO	22·87	22·80	25·77	25·91	25·82	25·28	25·25	SrO	0·95	3·97
CaO	n.d.	0·02	0·01	n.d.	0·04	0·01	0·02	Na_2O	0·79	1·33
Na_2O	2·15	2·19	2·82	2·58	2·64	2·62	2·08	La_2O_3	0·03	0·07
K_2O	7·19	7·07	7·04	7·06	6·74	6·84	6·83	Ce_2O_3	0·88	3·47
								Nd_2O_3	0·03	0·07
								F	1·39	2·24
								Cl	2·87	0·92
Total*	94·88	94·93	95·71	96·41	95·87	95·35	95·90	Total†	93·05	92·45
Mg-no.	92·82	92·87	94·43	93·80	94·08	94·20	92·98			
P	36·9	18·7	48·0	33·9	20·6	18·8	36·2	P	129717	139419
K	71711	72575	60747	79052	70997	69992	70189	K	110	89·7
Sc	0·99	1·10	1·31	1·30	0·88	0·91	1·60	Sc	2·42	0·79
Ti	15500	16408	890	2839	2096	1807	1736	Ti	23·5	<2·94
V	255	284	88·8	142	108	130	78·8	V	3·65	3·82
Ni	1808	1727	1744	2046	1813	1773	1905	Ni	12·1	3·97
Zn	23·4	22·1	35·8	38·2	31·7	32·1	69·5	Zn	1·19	0·96
Ga	11·1	9·84	n.a.	21·0	19·0	18·8	23·5	Ga	n.a.	n.a.
Rb	185	147	289	183	133	133	342	Rb	0·15	0·49
Sr	102	116	77·5	32·5	36·3	35·0	101	Sr	7138	42233
Y	0·10	0·086	<0·057	<0·054	0·021	0·006	0·052	Y	98·8	1454
Zr	0·19	0·19	0·43	<0·088	0·077	0·070	0·73	Zr	3·07	1·01
Nb	5·06	6·28	47·9	1·77	1·02	1·46	21·0	Nb	0·24	0·20
Cs	1·75	1·38	2·61	3·99	2·16	1·80	7·98	Cs	<0·013	<0·036
Ba	1212	1096	1343	298	277	219	1124	Ba	139	126
La	0·10	0·055	0·069	<0·029	0·020	<0·003	<0·045	La	7460	19048
Ce	0·027	0·011	<0·075	<0·019	0·14	<0·003	0·078	Ce	6844	25945
Pr	0·012	0·008	<0·067	<0·024	0·012	<0·003	<0·019	Pr	380	2212
Nd	0·019	0·035	<0·405	<0·079	0·065	<0·009	<0·224	Nd	749	6530
Sm	0·015	<0·011	<0·474	<0·090	0·016	<0·010	<0·132	Sm	51·5	747
Eu	0·022	0·017	<0·104	<0·026	0·013	0·010	<0·095	Eu	14·7	189
Gd	<0·010	<0·011	<0·43	<0·15	<0·011	0·012	0·17	Gd	31·4	451
Tb	<0·002	<0·002	n.a.	<0·027	0·002	<0·002	<0·028	Tb	n.a.	n.a.
Dy	<0·015	<0·017	0·45	<0·077	<0·007	<0·006	<0·077	Dy	19·8	281
Ho	<0·002	<0·003	<0·043	<0·020	0·002	<0·002	<0·028	Ho	3·59	51·1
Er	<0·009	<0·013	<0·25	<0·11	<0·016	<0·009	<0·11	Er	9·03	119
Tm	<0·002	<0·002	<0·088	<0·013	0·002	0·003	<0·018	Tm	1·19	13·8

(continued)

Table 5: Continued

Type:	III-b		III-c						III-b	III-c
Mineral:	phlog.	phlog.	phlog.	phlog.	phlog.	phlog.	phlog.		apatite	apatite
Sample:	1965/15	1965/15	1965/3	785	785	785	1965/25		1959/15	1965/3
Texture:	veinlet	interst.	in opx	in opx	with amph in m.p.	around chromite	incl. in amph		bleb in glass	interst. grain
Yb	<0·014	<0·011	<0·47	<0·15	<0·011	<0·019	<0·17	Yb	8·03	72·4
Lu	0·002	<0·002	<0·061	<0·014	<0·002	<0·002	<0·020	Lu	1·15	7·42
Hf	0·019	0·018	<0·25	<0·053	<0·012	<0·006	<0·19	Hf	<0·023	<0·120
Ta	0·20	0·22	1·40	0·031	0·012	0·009	0·23	Ta	<0·015	<0·075
Pb	5·46	5·86	1·25	1·08	0·83	0·98	1·43	Pb	43·6	5·77
Th	<0·004	<0·004	<0·080	0·043	0·088	0·056	<0·021	Th	2538	1305
U	0·012	0·011	0·069	<0·018	0·038	0·030	0·031	U	572	278

interst., interstitial; m.p., melt pocket; n.a., not analysed; n.d., not detected.

data (e.g. LaTourrette *et al.*, 1995) indicate that amphibole crystallization alone is unlikely to deplete the metasomatic agent to such a high degree in HREE. The same probably accounts for the extreme Nb depletion in amphiboles from Ke 785*, relative to the other Type III-c xenolith (Ke 1965/25; see also Ionov *et al.*, 2002).

Further, clinopyroxene, phlogopite and amphibole in the Type III-b sample Ke 1965/15, on one hand, all show strongly fractionated REE patterns (e.g. high La/Ce in amphibole; Fig. 10c) but, on the other hand, are characterized by a positive Ti anomaly, decoupled from other HFSE (e.g. Hf and Zr; Fig. 9b). Trace element fractionation during amphibole crystallization (i.e. formation of Type III-c amphibole dunites), however, should lower Ti contents in the remaining fluid or melt (e.g. Moine *et al.*, 2001).

Based on textures, mineralogy and dominant common compositional features, the hypothesis that Type III-b and -c xenoliths were metasomatized by completely independent metasomatic agents can be ruled out. Therefore, two other possibilities remain to account for the inconsistent observations described above: (1) inference of other phases, reactants or products, that are able to fractionate specific trace elements, present in the mantle beneath Marsabit but not present in the few investigated samples; (2) pre-metasomatic compositional heterogeneities, similar to the inherited HREE variation in Type III-a clinopyroxene (see above).

Garnet would be an important sink for HREE, but metasomatism occurred in the spinel field, after decompression, with maximum pressures of <1·5 GPa (Kaeser *et al.*, 2006), so garnet had already broken down to symplectites (Fig. 15). Percolation of melt through garnet-bearing websterites, prior to metasomatism in Ke 1965/1 and 1965/15, could be an alternative. Websterites have been interpreted to occur in close spatial relationship with porphyroclastic peridotites in the shallow mantle beneath Marsabit (Kaeser *et al.*, 2006), and they occasionally contain rutile and ilmenite, which could further account for the strong Nb and Ta depletion in some samples (e.g. Ke 785*). The available compositional data from the websterites, however, do not indicate metasomatic modification of websteritic garnet (Olker, 2001; B. Kaeser, unpublished data) nor compositional similarities to Group III peridotites.

Careful study by SEM rules out the presence of exotic phases such as zircon or Ti-oxides, described from other xenolith suites (e.g. Bodinier *et al.*, 1996; Rudnick *et al.*, 1999). Nevertheless, it cannot be excluded that the metasomatizing agent percolated through mantle domains containing these phases before infiltrating the studied rocks.

The preservation of pre-metasomatic compositional heterogeneities is another possibility that must be considered. That such 'rock signals' partly overlap with the 'metasomatic signal' is indicated by the HREE variation in Type III-a clinopyroxene (see above) and also by other compositional parameters. For example, both Mg-katophorite and phlogopite growing at the expense of spinel have very high Cr_2O_3 contents, whereas euhedral Mg-katophorite in the amphibole dunite (Ke 1965/25) or in phlogopite inclusions in Opx_m is comparably Cr_2O_3-poor (Fig. 8b; Tables 4 and 5). Pre-existing heterogeneities would essentially be preserved through elements that are relatively compatible in a given mineral (i.e. that are not mobilized during metasomatism). This would be in agreement with the preserved HREE variations in Type III-a clinopyroxene, high Cr_2O_3 in amphiboles and phlogopite, and Ti spikes in amphibole from Ke 1965/15.

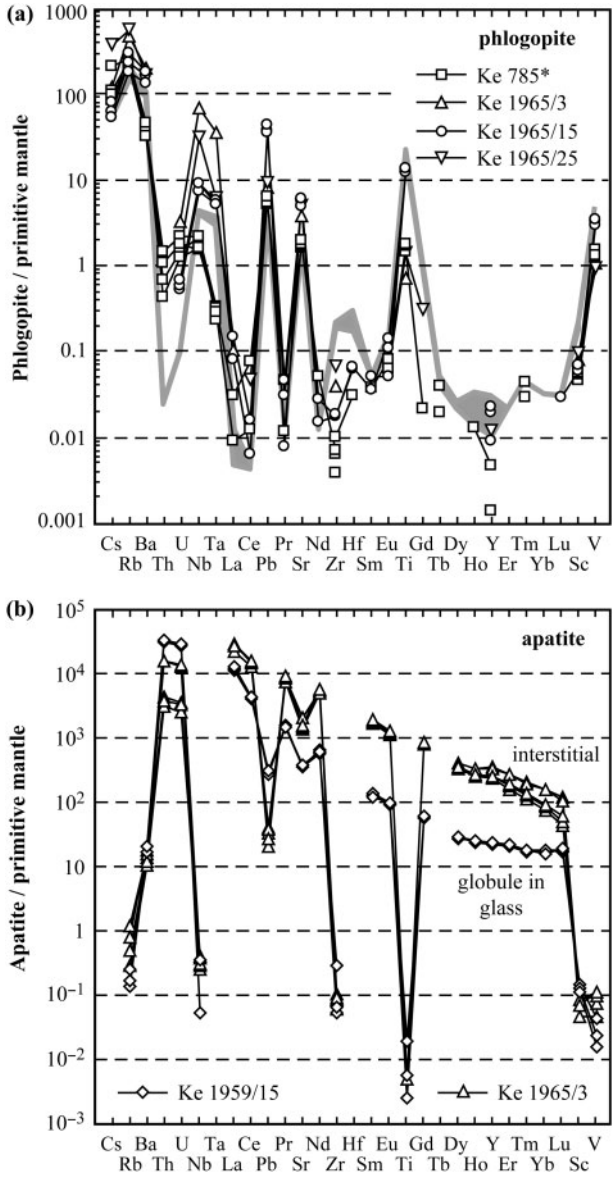

Fig. 11. Trace element patterns of (a) phlogopite and (b) apatite from porphyroclastic spinel harzburgites and dunites from Marsabit [concentrations normalized to the primitive mantle values of McDonough & Sun (1995)]. The grey field in (a) indicates the composition of Ti-rich phlogopite in Group I (grt)–spl lherzolites (Kaeser *et al.*, 2006).

Further, very high Mg-numbers in replacive amphiboles support melt (fluid)–rock interaction at low melt (fluid)/rock ratios, where Mg and Fe contents are buffered by the ambient peridotite (Kelemen *et al.*, 1995; Tiepolo *et al.*, 2001). The slightly lower Mg-number of euhedral amphiboles in Ke 1965/25, combined with their lower Cr_2O_3 contents (Fig. 8b), suggests a higher melt (fluid)/rock ratio, which is further supported by considerably lower Mg-number in associated ol-I (~Fo88; Table 3).

The limited number of investigated samples does not allow us to decide which of the processes described above acted, and to what extent. However, given the heterogeneity observed in the numerous non-metasomatized xenoliths from Marsabit (Kaeser *et al.*, 2006), pre-metasomatic features certainly affect the final product of the melt–rock reaction process to a considerable degree.

The nature of the metasomatizing agent(s)

Graphite stability and oxygen fugacity considerations

The Marsabit xenoliths are unusual in that they occur in an off-cratonic setting yet bear macroscopic graphite. The latter usually either occurs in kimberlite-hosted peridotites (on-craton) or in pyroxenites from alpine-type peridotite bodies (e.g. Pearson *et al.*, 1994). In the phlogopite peridotites from Finero, graphite has recently been reported as nanoscopic layers in phlogopite (Ferraris *et al.*, 2004). In xenoliths from Marsabit, graphite occurs in the same textural relationship as in kimberlite-hosted peridotite xenoliths (i.e. millimetre-sized flakes, typically associated with orthopyroxene; see Fig. 3c–e and Pearson *et al.*, 1994). Graphite inclusions in phlogopite and Opx_m could indicate crystallization during metasomatism by a 'reduced' C-bearing fluid or melt. However, precipitation of graphite more probably reflects the relatively reducing conditions in the uppermost mantle prior to metasomatism. We used the oxygen barometer of Ballhaus *et al.* (1991), based on ferric iron contents in spinel coexisting with olivine, to constrain oxygen fugacity (fO_2) conditions prior to metasomatism in the Marsabit xenoliths (Fig. 16). The results show that non-metasomatized Group I and IV samples reflect similarly reducing conditions to the cryptically metasomatized Type III-a samples.

Although assessing Fe^{3+}/Fe^{2+} ratios in spinel based on microprobe analyses can be problematic (Wood & Virgo, 1989; Ballhaus *et al.*, 1991), all microprobe analyses were obtained using the same operational settings and, therefore, give at least the relative fO_2 variation between samples. The relatively reducing conditions in the pre-metasomatic, cold and highly deformed mantle, well below carbon–carbonate–silicate equilibria ($Mg_2Si_2O_6 + 0{\cdot}5\ CaMg(CO_3)_2 = Mg_2SiO_4 + 0{\cdot}5\ CaMgSi_2O_6 + C + O_2$; Eggler & Baker, 1982; see Fig. 16) and close to the CCO oxygen buffer are in agreement with the presence of graphite in the Group III harzburgites. Moreover, the P–T conditions at which the Group III xenoliths partially re-equilibrated are close to the subsolidus decarbonation of model carbonated lherzolite (Fig. 2; see Lee & Wyllie, 2000, and references therein), in agreement with the observed phase assemblage including orthopyroxene, olivine, clinopyroxene and graphite.

Table 6: Representative analyses of silicate glass (oxides in wt%; trace elements in μg/g)

Type:	III-b			III-c						Host
Sample:	1959/15	1965/15	1965/15	785*	1965/25	1965/3	1965/3	1965/3	1959/27	
Remark:	next amph	next cpx	xenol. margin	next amph	next amph	melt pocket	next apatite	next Opx_m	melt pocket	host basanite*
SiO_2	53·06	57·75	51·61	60·96	56·57	59·38	59·74	65·30	48·82	44·10
TiO_2	0·17	1·57	1·06	0·62	0·30	0·24	0·20	0·23	3·78	2·55
Al_2O_3	24·12	20·53	20·25	17·79	23·13	15·75	12·45	13·55	18·90	13·96
Cr_2O_3	0·05	0·01	n.d.	0·01	0·01	n.d.	n.d.	n.d.	0·02	n.a.
$FeO_{(tot)}$	1·88	2·47	6·26	1·26	2·52	2·95	3·74	2·65	5·09	12·83
MnO	0·07	0·00	0·26	0·01	0·04	0·05	0·08	0·07	0·18	0·21
NiO	n.d.	n.d.	n.d.	n.a.	n.d.	n.a.	0·06	n.d.	0·01	n.a.
MgO	1·82	1·29	1·16	1·14	1·22	3·04	3·82	2·52	2·44	9·38
CaO	5·06	2·57	2·83	0·82	0·44	1·24	1·01	0·39	8·10	10·30
Na_2O	11·07	9·66	9·69	9·71	12·99	13·88	13·84	12·11	6·73	3·74
K_2O	1·54	1·97	4·65	3·57	1·38	1·21	1·42	1·27	3·00	1·46
Cl	0·31	1·06	0·38	0·12	0·14	0·23	0·61	0·20	0·15	n.a.
P_2O_5	0·41	0·08	0·44	0·09	0·12	0·49	2·33	0·18	1·00	0·59
Total	99·56	98·96	98·60	96·09	98·87	98·45	99·29	98·46	98·21	99·12
Mg-no.	63·29	48·16	24·89	61·75	46·32	64·74	64·58	62·89	45·52	56·58
P	1061	448	1610	230	503	1519	6738	676	2994	n.a.
K	12563	16408	39599	32515	15872	9265	11277	10071	25900	n.a.
Sc	1·79	1·84	1·26	4·06	1·51	9·70	13·6	8·48	6·91	23·7
Ti	665	7329	4974	2953	1965	1213	1163	1055	18199	15311
V	107	26·5	23·5	79·6	92·0	210	151	134	234	n.a.
Ni	12·8	37·1	9·2	<5·75	9·83	17·0	<19·9	<29·8	19·9	191
Zn	9·62	10·3	109	11·0	45·9	44·0	50·8	30·9	81·9	n.a.
Ga	n.a.	17·3	27·3	19·4	22·0	n.a.	n.a.	n.a.	n.a.	n.a.
Rb	18·1	26·3	124	54·6	6·26	17·6	39·8	36·9	57·7	36·9
Sr	427	488	1407	188	881	1644	4997	985	1062	792
Y	5·43	1·45	22·4	7·52	26·2	61·9	158	36·9	30·1	29·9
Zr	4·66	17·1	353	7·61	66·0	57·8	36·5	42·8	242	216
Nb	4·16	16·1	137	2·60	136	234	164	169	83·7	64·7
Cs	0·14	0·46	1·86	1·25	0·07	0·22	1·02	0·52	0·63	n.a.
Ba	238	261	1064	129	168	405	1099	641	625	563
La	69·8	18·3	84·8	14·4	88·9	221·2	1008	106	53·7	46·2
Ce	94·7	25·6	131	30·8	138	333	1265	164	104	82·3
Pr	6·55	1·94	12·0	3·30	11·6	30·4	97·5	16·0	12·0	n.a.
Nd	14·6	6·03	40·8	10·1	32·9	99·3	256	56·4	46·3	40·0
Sm	1·42	0·48	5·70	1·79	4·19	14·1	37·9	6·79	10·5	8·51
Eu	0·41	0·35	2·28	0·82	1·12	4·38	10·3	2·41	3·45	2·67
Gd	0·62	0·51	4·15	1·58	4·02	10·6	24·5	5·66	6·77	7·29
Tb	n.a.	0·086	0·86	0·20	0·71	n.a.	n.a.	n.a.	n.a.	1·11
Dy	0·90	0·27	3·59	0·98	4·34	10·4	17·1	6·37	7·32	n.a.
Ho	0·23	0·037	1·05	0·25	0·95	2·06	4·46	1·04	1·17	1·14
Er	0·45	0·38	1·95	0·58	2·55	6·11	15·3	2·64	3·05	n.a.
Tm	0·09	<0·039	0·33	0·081	0·42	0·85	2·92	<0·14	0·36	0·52
Yb	0·62	0·23	2·67	0·44	3·07	6·67	12·0	4·87	2·53	2·20

(continued)

Table 6: Continued

Type:	III-b			III-c						Host
Sample:	1959/15	1965/15	1965/15	785*	1965/25	1965/3	1965/3	1965/3	1959/27	
Remark:	next amph	next cpx	xenol. margin	next amph	next amph	melt pocket	next apatite	next Opx_m	melt pocket	host basanite*
Lu	0·14	0·050	0·26	0·041	0·46	0·80	1·40	0·58	0·40	0·31
Hf	0·26	0·52	5·35	0·14	0·76	1·10	<0·87	1·24	5·68	5·04
Ta	<0·080	0·33	6·38	0·022	1·23	10·1	7·84	8·01	3·94	4·03
Pb	5·41	44·8	28·0	2·55	8·40	7·97	26·0	7·49	4·93	n.a.
Th	19·4	2·96	16·0	4·66	7·03	18·5	247	10·5	5·34	5·06
U	5·45	0·69	4·78	0·99	1·52	4·47	72·4	2·16	1·71	1·26

n.d., not detected; n.a., not analysed.
*Average composition of the strongly alkaline basanites from Marsabit (Volker, 1990).

Evidence for low-temperature SiO_2–Na_2O–CO_2–H_2O-rich melts or fluids

Potential metasomatic agents, inferred from the presence of graphite, are C–O–H-rich fluids, carbonate melts or CO_2-bearing silicate melts. The resulting phase assemblages and geochemical signatures are the result of infiltration of fluid or melt into a cold (~750–850°C), shallow (<1·5 GPa; Fig. 2), heterogeneous and locally reduced lithospheric mantle. Metasomatism under such conditions in an open system must result in complex geochemical signatures that reflect the degree of fluid–rock reaction. This makes it particularly difficult to constrain the exact nature of the 'original' metasomatic agent.

Type III-c xenolith Ke 1965/25 contains the highest fraction of metasomatic phases and the least fractionated amphibole trace element patterns. The 'magmatic' textures of the Mg-katophorites in this sample suggest direct crystallization from a melt or a fluid rather than replacement of a pre-existing phase. Therefore, hypothetical liquids in equilibrium with the amphiboles in this xenolith could yield the composition of the initial metasomatic agents. Figure 17 illustrates the trace element patterns of such melts and fluids, calculated using sets of experimentally or empirically determined mineral/melt (fluid) partition coefficients, including carbonate melt, silicate melt and hydrous fluid (for references see caption to Fig. 17).

Common features for all calculated metasomatic agents are negative Zr–Hf–Ti anomalies and LREE enrichment (Fig. 17). However, previous studies have shown that these signatures are indicative of almost all types of metasomatism, including interaction of peridotite with carbonatitic melt (Green & Wallace, 1988; Dautria *et al.*, 1992; Hauri *et al.*, 1993; Rudnick *et al.*, 1993; Ionov *et al.*, 1996; Yaxley *et al.*, 1998; Coltorti *et al.*, 1999), with hydrous fluids and/or melts, for example, originating from dehydration of altered subducting lithosphere (Maury *et al.*, 1992; Zanetti *et al.*, 1999; Grégoire *et al.*, 2001; Laurora *et al.*, 2001; Parkinson *et al.*, 2003), and interaction of peridotite with volatile- and Si-rich melts that evolved through reactive porous flow (Bedini *et al.*, 1997; Ionov *et al.*, 2002, 2006; Bodinier *et al.*, 2004; Rivalenti *et al.*, 2004).

In the case of the Marsabit xenoliths, integration of the trace element characteristics, thermobarometric inferences and mineralogical constraints favours a Na_2O–SiO_2–CO_2–H_2O-rich silicate melt. Carbonated melts can probably be ruled out on major element and mineralogical considerations. First, amphiboles are Ca-poor, in conflict with carbonate melt metasomatism, which is generally characterized by Ca enrichment (Rudnick *et al.*, 1993; Neumann *et al.*, 2002). Further, orthopyroxene is a stable phase and probably even crystallizes during metasomatism in some samples (e.g. Ke 785*). At near-solidus conditions coexistence of orthopyroxene and carbonate melt is possible only at pressures ≥2·0 GPa (see Fig. 2; e.g. Lee & Wyllie, 2000, and references therein), which is considerably higher than the maximum pressures indicated by the composition of spinel (<1·5 GPa). At such low pressures, metasomatism by carbonated melts will convert lherzolite and harzburgite immediately into wehrlite, which is the major peridotite type in all xenolith suites where carbonate melt metasomatism is convincingly demonstrated (Rudnick *et al.*, 1993; Yaxley *et al.*, 1998; Neumann *et al.*, 2002). In Marsabit, wehrlites are absent, however.

An Na_2O–SiO_2–CO_2–H_2O-rich melt or fluid, on the other hand, would explain the Na-rich nature of amphibole and phlogopite, as well as the presence of orthopyroxene. Growth of metasomatic (and Al-poor) orthopyroxene has been described from several xenolith localities where peridotites were infiltrated either by hydrous fluids or Si-rich melts (Smith *et al.*, 1999; McInnes *et al.*, 2001; Morishita *et al.*, 2003). Na-rich phlogopite is commonly

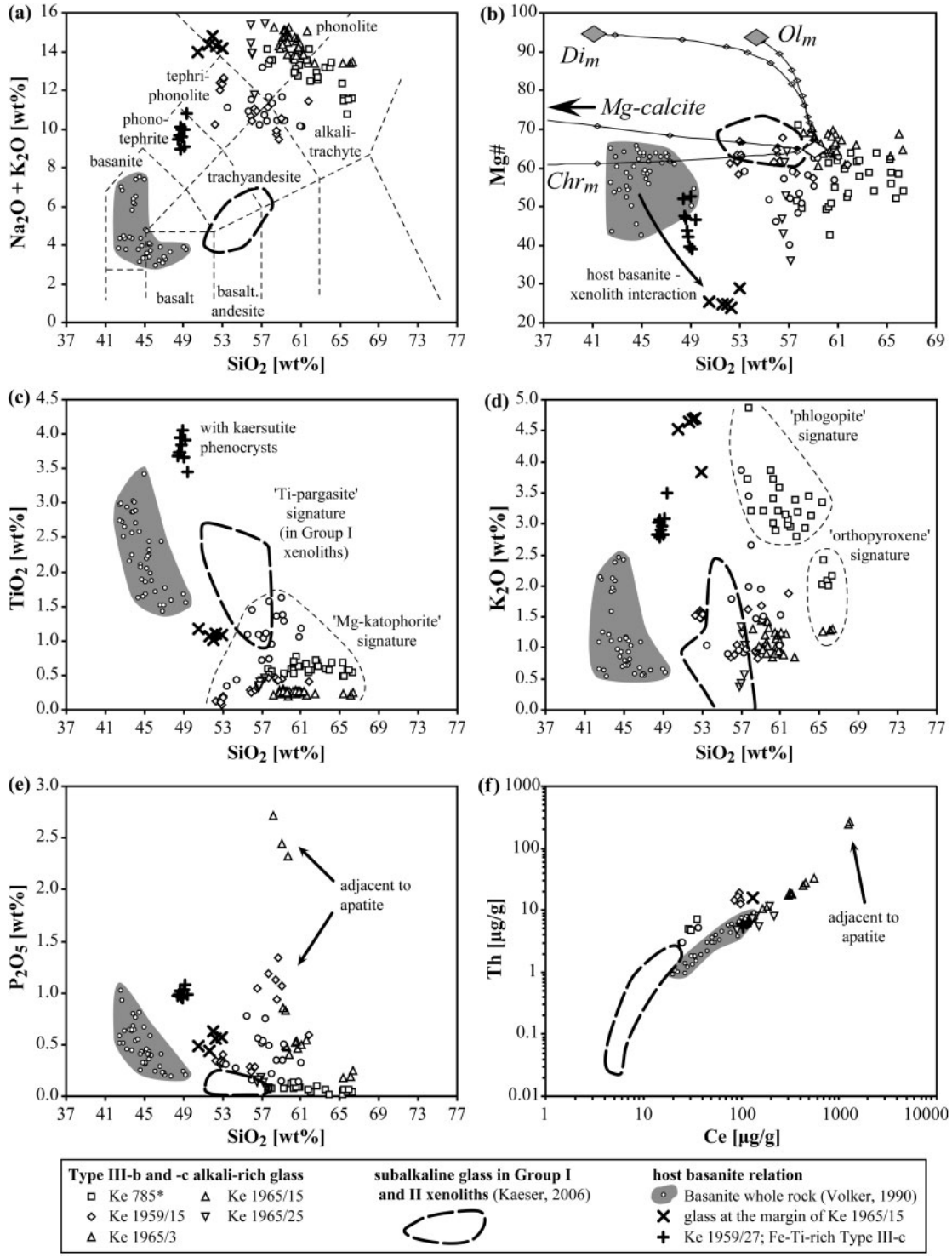

Fig. 12. Total alkalis vs SiO_2 (a), Harker-type co-variation diagrams (b–e) and incompatible trace element co-variation diagram (f), showing the compositional variability of silicate glass found in the porphyroclastic spinel harzburgites and dunites from Marsabit. In (b) binary mixing lines between the typical composition of the alkali-rich glass (large open diamond) and the associated microlites are shown (each increment is 10 wt%). They illustrate that the glass does not represent the derivate of host lava infiltration and fractional crystallization. Subalkaline glass in Group I (grt)–spl lherzolites from Marsabit is shown for comparison and is interpreted to derive from incongruent melting of Ti-pargasite (Kaeser, 2006).

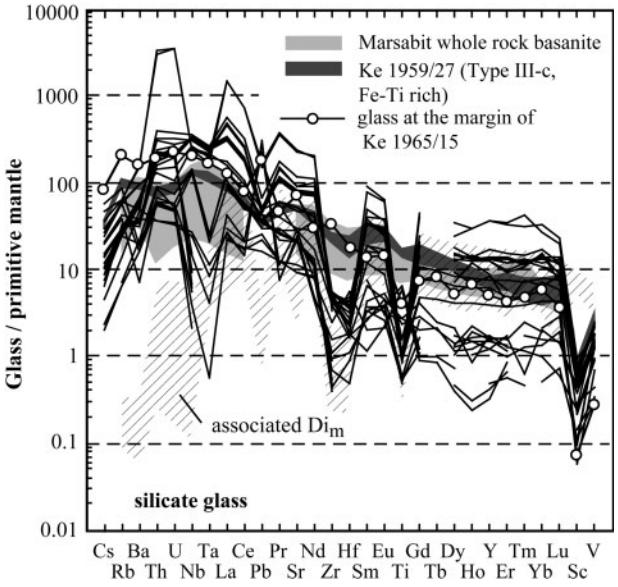

Fig. 13. Trace element patterns of silicate glass in porphyroclastic spinel harzburgites and dunites from Marsabit compared with the trace element composition of associated clinopyroxene (Di_m) micro-phenocrysts, xenolith-hosting basanites from Marsabit and glass interpreted to represent xenolith–host interaction [concentrations normalized to the primitive mantle values of McDonough & Sun (1995)].

found as a reaction product between anhydrous mafic to ultramafic rocks and H_2O-rich evolved liquids (Costa *et al.*, 2001, and references therein) or H_2O-bearing fluids (e.g. Odling, 1994). The latter study was an experiment at 2·0 GPa simulating the effects of decreasing temperatures on the phase assemblages and their composition during metasomatism using a model peridotite + C–O–H fluid. The coolest part of Odling's (1994) experiment (<1075°C) contained a strikingly similar phase assemblage (katophorite, phlogopite with ~2 wt% Na_2O, and Al-poor orthopyroxene) to the Marsabit samples, interpreted to have formed during sub-solidus fluid–solid interaction. A compositionally similar phase assemblage (high amounts of opx, Si-rich hornblende, Na-rich phlogopite) resulted from experiments simulating peridotite interaction with Si-rich melt (dacite) at lower P–T conditions (950°C at 0·92 GPa; Prouteau & Scaillet, 2003).

In this study, the trace element signatures of Group III-c Mg-katophorite and the calculated metasomatic agents further suggest that the metasomatizing agent was a melt rather than a fluid. Hypothetical fluids in equilibrium with euhedral Mg-katophorite from sample Ke 1965/25 have high Nb/LILE (e.g. Rb, Ba) and low LILE/REE ratios (Fig. 17). Because experimental data predict the opposite for fluids (LILE enriched over HFSE and REE; e.g. Manning, 2004, and references therein), a fluid with a signature such as that indicated in Fig. 17 is unrealistic.

Table 7: Representative analyses of carbonates (oxides in wt%; trace elements in μg/g)

Group:	III-b	III-b	III-c	III-c	III-c
Mineral:	Dol	Mg-Cc	Mg-Cc	Mg-Cc	Mg-Cc
Sample:	1959/15	1965/15	785*	1965/3	1965/3
Texture:	in glass	in glass	in glass	in glass	in glass
SiO_2	n.a.	0·03	n.a.	n.d.	0·03
$FeO_{(tot)}$	0·16	0·11	0·10	0·10	0·06
MnO	0·01	n.d.	n.d.	n.d.	n.d.
MgO	19·22	2·36	1·90	1·25	5·17
CaO	31·89	53·13	53·77	53·91	48·53
Na_2O	0·03	n.d.	0·04	n.d.	0·03
K_2O	n.a.	0·02	n.a.	0·01	n.d.
SrO	0·03	0·10	0·08	0·04	0·21
BaO	0·03	n.d.	n.d.	n.a.	n.a.
CO_2[1]	46·18	44·44	44·42	43·77	43·91
Total	97·56	100·21	100·32	99·09	97·94
Mg-no.	99·54	97·45	97·13	95·54	99·31
Ca-no.	54·39	94·18	95·31	96·87	87·09
P	220	334	137	580	589
K	9·70	21·2	6·42	10·5	15·5
Sc	<0·65	<0·150	0·27	<0·27	<0·076
Ti	9·75	18·9	24·2	5·28	1·96
V	<0·85	0·481	<0·42	<0·37	0·21
Ni	9·00	6·73	5·17	<2·94	5·93
Zn	4·59	<0·89	1·13	2·96	0·45
Ga	n.a.	<0·14	<0·13	n.a.	n.a.
Rb	0·084	<0·072	<0·074	<0·060	0·046
Sr	593	860	371	251	4274
Y	0·12	0·11	1·30	7·04	0·15
Zr	2·61	0·24	0·12	0·97	7·56
Nb	1·44	0·19	0·056	6·92	1·85
Cs	<0·063	<0·011	<0·018	<0·039	<0·008
Ba	1·26	2·30	<0·24	0·29	27·1
La	0·34	0·57	0·84	13·6	0·25
Ce	0·32	0·13	1·34	9·97	0·23
Pr	0·06	0·06	0·18	0·95	0·026
Nd	0·30	0·13	0·68	2·28	0·078
Sm	<0·44	<0·091	0·074	0·48	<0·018
Eu	<0·12	<0·019	0·051	0·20	<0·008
Gd	<0·37	<0·090	0·14	0·51	0·026
Tb	n.a.	<0·010	0·036	n.a.	n.a.
Dy	<0·19	<0·039	0·089	0·58	<0·038
Ho	<0·029	0·013	0·044	0·11	<0·006
Er	<0·12	<0·041	0·083	0·33	<0·019
Tm	<0·052	<0·013	0·016	0·084	<0·006
Yb	<0·43	<0·063	0·14	0·27	<0·040
Lu	<0·072	<0·010	0·011	0·066	<0·008

(continued)

Table 7: Continued

Group:	III-b	III-b	III-c	III-c	III-c
Mineral:	Dol	Mg-Cc	Mg-Cc	Mg-Cc	Mg-Cc
Sample:	1959/15	1965/15	785*	1965/3	1965/3
Texture:	in glass	in glass	in glass	in glass	in glass
Hf	<0·16	<0·038	<0·036	<0·074	<0·013
Ta	0·048	<0·012	<0·016	<0·031	0·008
Pb	<0·24	8·58	<0·21	0·74	0·18
Th	0·021	<0·020	<0·017	<0·028	<0·005
U	0·60	0·94	0·86	6·00	1·48

Mg-Cc, Mg-calcite; Dol, dolomite; n.d., not detected; n.a., not analysed; Ca-number = 100 × Ca/(Ca + Mg).
[1]Calculated from stoichiometry.

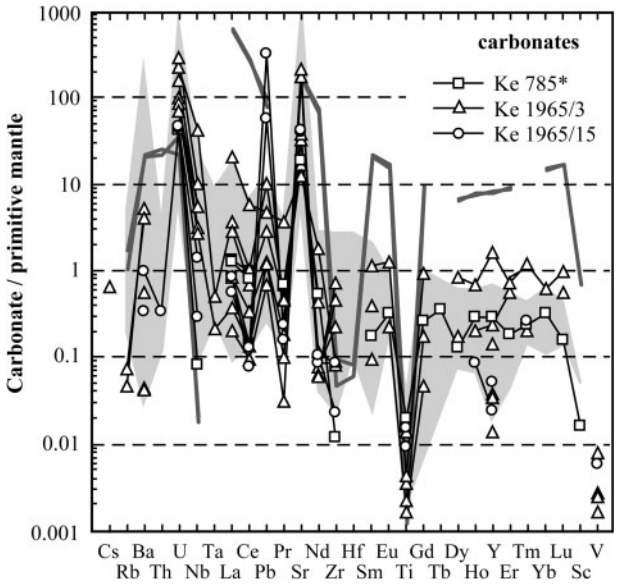

Fig. 14. Trace element patterns of glass-hosted carbonates in Type III-b and -c spinel harzburgite and dunite xenoliths from Marsabit [concentrations normalized to the primitive mantle values of McDonough & Sun (1995)]. The grey field outlines the compositional range of carbonates found in other peridotite xenoliths (Ionov & Harmer, 2002, and references therein). Carbonate material interpreted as quenched carbonatite melt, found in peridotite xenoliths from Kerguelen (Moine *et al.*, 2004) is shown for comparison (bold line).

At the relatively low maximum pressures (<1·5 GPa), a supercritical liquid is not expected either (e.g. Kessel *et al.*, 2005).

Finally, a relatively hydrous metasomatizing agent would be consistent with formation of Mg-katophorites with low Ti and presumably low Fe^{3+} contents (given the relatively reducing conditions), which, in turn, imply high $(OH)^-$ contents. In other words, partial dehydrogenation, typically observed in common (Ti-rich) mantle amphibole (e.g. Popp *et al.*, 1995; Tiepolo *et al.*, 2001, and references therein), cannot have played an important role in this case, as H deficiency is mainly the result of coupled substitutions involving Ti and Fe^{3+} (Popp *et al.*, 1995). In conclusion, the metasomatizing agent was most probably a Na_2O–SiO_2–CO_2–H_2O-rich melt.

Comparison with experimental studies further constrains the low-temperature regime in which metasomatism occurred. In ultramafic (e.g. Niida & Green, 1999), basaltic (e.g. Rapp, 1995) and Si-enriched systems (e.g. trachybasaltic; Barclay & Carmichael, 2004) amphibole (in the latter study together with phlogopite) is confined to temperatures lower than 1000–1050°C at pressures <2·0 GPa (Fig. 2). Thus, crystallization of the early metasomatic phase assemblage can be explained by infiltration of a silicate melt that rapidly cooled upon contact with the ambient peridotite (~750–850°C prior to metasomatism; Fig. 2). However, this low-T stage is based on Ca-in-opx thermometry (see Brey & Köhler, 1990; Kaeser *et al.*, 2006; Table 1) and therefore probably underestimates the effective temperature conditions during metasomatism. This can be explained by low diffusion rates and proximity to the closure temperature for the diopside–enstatite exchange reaction at temperatures lower than 850°C (e.g. Smith, 1999, and references therein). The lower temperature limit at which silicate melt metasomatism is possible (i.e. defined by the melt's solidus and viscosity) depends strongly on volatile and SiO_2 contents. Experiments by Draper & Green (1997), for example, showed that highly silicic melts (~52–64 wt% SiO_2) can be in equilibrium with mantle harzburgite at temperatures as low as 850°C (at 1·0–2·0 GPa; under anhydrous and C–O–H-fluid-bearing conditions). These are, however, extreme compositions for mantle melts. The actual SiO_2 content of the metasomatizing agent in this case is difficult to constrain from the metasomatic mineral assemblage, as compositions may have varied considerably during reactive percolation (e.g. including Si-releasing reactions such as cpx replacement by amphibole versus Si-consuming reactions such as Opx_m crystallization). Moreover, it is unlikely that a melt persists at temperatures much below ~900°C, which is the solidus of fertile lherzolite (i.e. primitive upper mantle composition) under H_2O-saturated conditions at 1·5 GPa (Grove *et al.*, 2006; see Fig. 2). Below the solidus, residual volatile-enriched fluids may percolate further; for example, forming the less metasomatized Type III-c xenoliths (e.g. Ke 785*), as well as Type III-b and -a peridotites (see also Bailey, 1987). Relatively cold conditions would also explain the very high compositional gradients developed on small scales in Type III-a samples (Fig. 15). Given the absence of chlorite in all investigated samples, the lower temperature limit of such fluid metasomatism is ~800°C (e.g. Fumagalli & Poli, 2005; see Fig. 2).

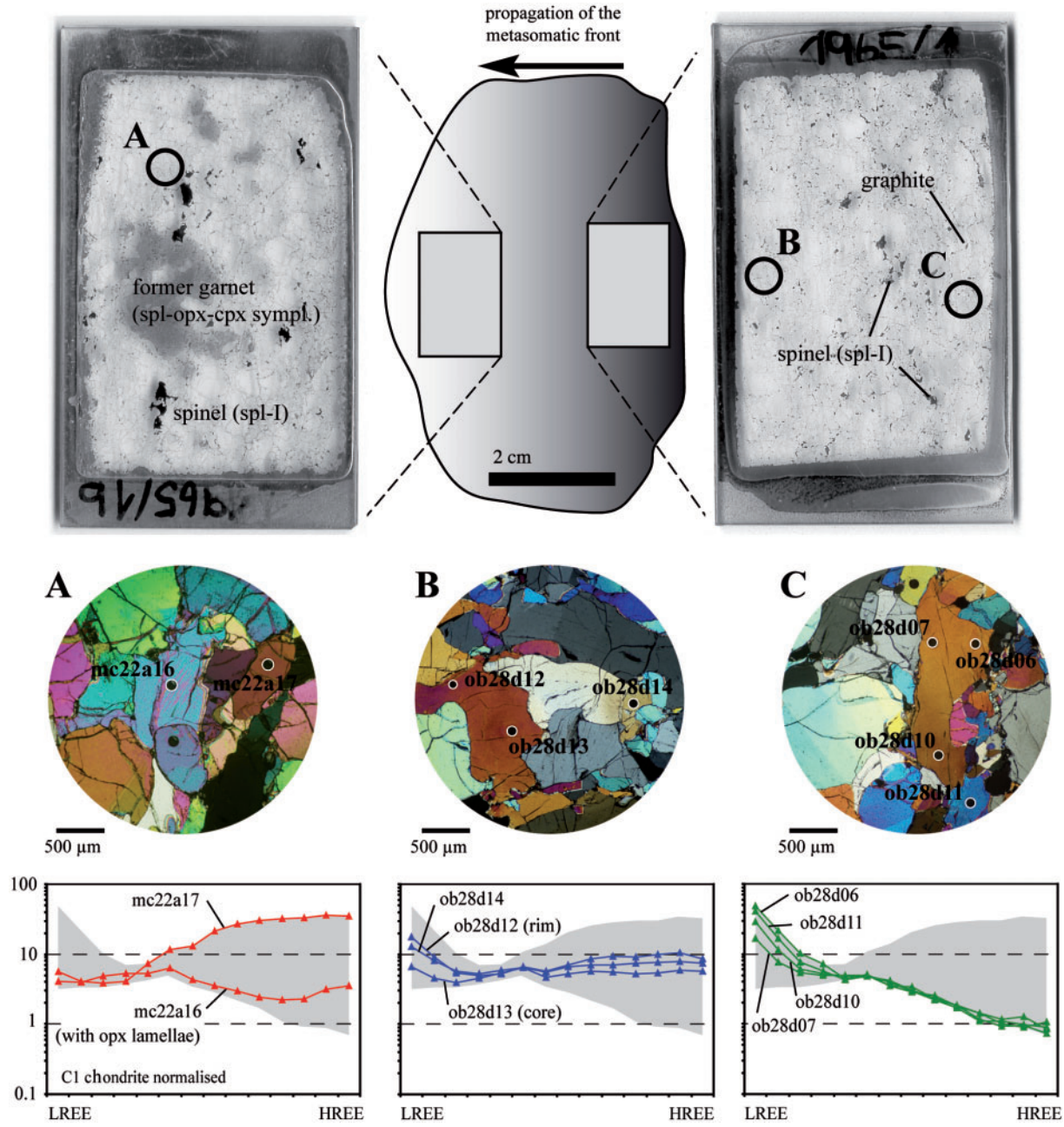

Fig. 15. Detailed REE systematics in primary clinopyroxene (cpx-I) in a porphyroclastic, cryptically metasomatized spinel harzburgite (sample Ke 1965/1) showing the transition from Type III-a (Zone A and B) to Type III-b (Zone C) on a scale of a few centimetres. The numbers on the photomicrographs (crossed polars) correspond to single laser ablation microprobe pits (for further explanation, see text).

Finally, the presence of apatite, even though often taken as indicator for carbonatite-type metasomatism (e.g. Yaxley *et al.*, 1998), is not in conflict with metasomatism by silicate melts. Apatite has also been shown to crystallize from volatile and alkali-rich derivatives formed during reactive porous flow of originally mafic silicate melts (Woodland *et al.*, 1996; Bedini *et al.*, 1997; Bodinier *et al.*, 2004; Ionov *et al.*, 2006).

FORMATION OF THE LATE, GLASS-BEARING ASSEMBLAGES

Textures strongly suggest that the glass-bearing assemblages formed later and at the expense of the early metasomatic assemblages (Fig. 4a and d). Features such as the reappearance of clinopyroxene (Na-rich Cr diopside micro-phenocrysts), a phase replaced by the early

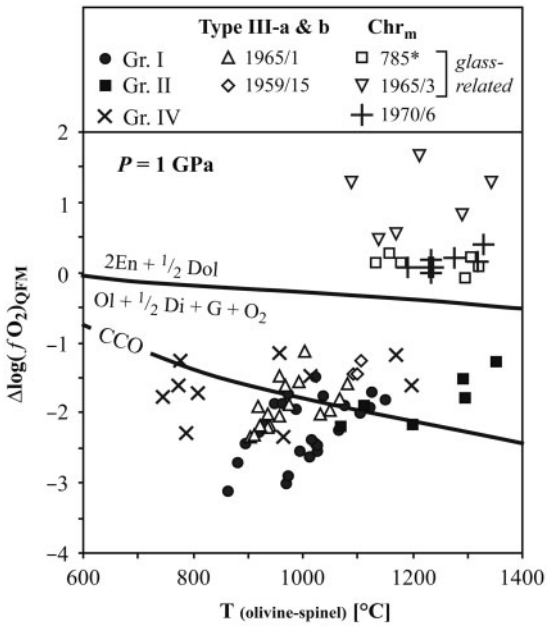

Fig. 16. Oxygen fugacities relative to the quartz–fayalite–magnetite buffer (QFM; equation of O'Neill, 1987) as a function of temperature at assumed pressure of 1 GPa calculated using the composition of coexisting spinel and olivine (ol-I–spl-I pairs and Chr_m–Ol_m pairs, respectively) based on the oxygen barometer of Ballhaus *et al.* (1991). The graphite–CO_2 equilibrium was calculated after Frost & Wood (1998), and the graphite–carbonate–silicate equilibrium was calculated using the equation of Eggler & Baker (1982). (See text for further explanation.)

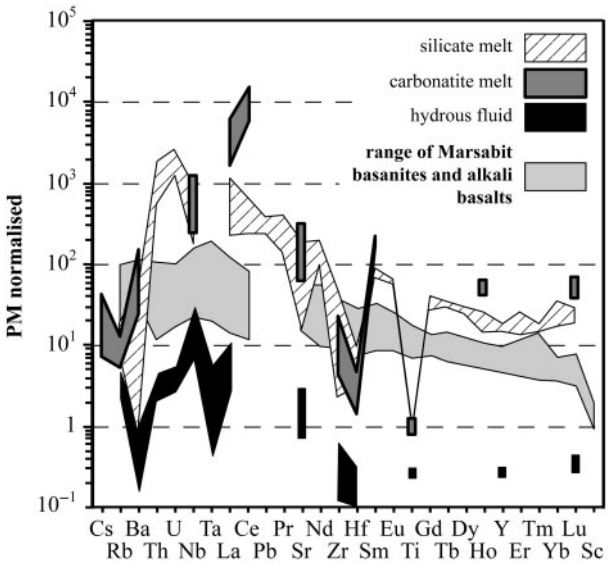

Fig. 17. Calculated metasomatic agents in equilibrium with the euhedral Mg-katophorites from the Type III-c amphibole dunite Ke 1965/25. Amphibole/hydrous fluid and amphibole/carbonatite melt partition coefficients are from Adam *et al.* (1997) and Adam & Green (2001), respectively. Silicate melts have been calculated using amphibole/Si-rich melt partition coefficients from Chazot *et al.* (1996*b*) and amphibole/basanite partition coefficients from LaTourrette *et al.* (1995). The compositional range of the Marsabit basanites and alkali basalts (Volker, 1990) is shown for comparison.

metasomatic assemblage, indicate that melt pocket formation reflects a significant change in P–T–X space in parts of the mantle beneath Marsabit after earlier metasomatism. Based on geochemical arguments and mass-balance considerations, we will show that (1) the late, glass-bearing assemblages are closely related to early metasomatic assemblages, mainly representing breakdown products, and (2) breakdown was induced by infiltration of a CO_2-rich fluid in the mantle, probably followed and enhanced by heating and decompression melting during xenolith transport in the host magma.

Evidence for *in situ* partial melting

BSE imaging reveals that the phases becoming unstable are amphibole, orthopyroxene and, to minor extents, spl-I, phlogopite, cpx-I and apatite. Compositional (inter- and intra-xenolith) heterogeneity of silicate glass is texture controlled and varies as a function of the associated precursor phases (Fig. 12a–f). TiO_2, for example, shows higher concentrations in glass from xenolith Ke 1965/15 containing Ti-enriched amphibole (Fig. 12c), whereas K_2O contents are highest in phlogopite-rich samples (e.g. Ke 785*; Fig. 12d). Elevated P_2O_5 contents are found in glass adjacent to apatite (Fig. 12e), which mirrors at the same time the high Th and LREE contents of apatite (Fig. 12f). Significant Si enrichment is found in glass coating orthopyroxene (Fig. 12d), supporting incongruent melting of orthopyroxene (see below). Even though the melt pockets are connected along grain boundaries, the strong compositional variation (on inter- and intra-xenolith scale) suggests that the mobility of the melt was limited, or that the melting event was very short-lived (for timing constraints see below).

The co-variation plots in Fig. 12 further reveal considerable compositional differences between all types of xenolith glass and the host basanite. These data indicate that the glass cannot be the product of xenolith–host lava interaction during ascent to the surface. Also, back-mixing of micro-phenocrysts into the melt fails to derive the glass from a host-related melt (Fig. 12b). Glass from xenolith margins, however, is compositionally closer to the bulk host basanite (e.g. Fig. 12b), in line with a direct derivation from xenolith–host lava interaction. Its more evolved major element composition (e.g. higher SiO_2, lower Mg-number; Fig. 12b) is probably the result of fractionation of basanite phenocrysts (e.g. olivine, augite and titanomagnetite; Volker, 1990). Host lava–xenolith interaction is further supported by the trace element signature of glass at the margin of the xenoliths, which is closely similar to that of the Marsabit basanites (Fig. 13; Volker, 1990). The same characteristics are observed for intra-xenolith glass in the unusual kaersutite-bearing sample Ke 1959/27.

Xenolith glass unrelated to the host lava and melt pockets similar to those reported here, in association with residual phases (e.g. amphibole or clinopyroxene), has been reported from many xenolith localities (e.g. Frey & Green, 1974; Ionov *et al.*, 1994, 1996; Chazot *et al.*, 1996*a*, 1996*b*; Yaxley *et al.*, 1997; Laurora *et al.*, 2001; Bali *et al.*, 2002). Residual phases within the melt pockets strongly indicate *in situ* partial melting within the xenoliths. However, a variety of processes may trigger such *in situ* melting, including: (1) closed-system decompression melting of either anhydrous (Maaløe & Printzlau, 1979) or hydrous phases (Frey & Green, 1974; Francis, 1976) during xenolith ascent in the host lava; (2) melting during interaction of the xenoliths with the host basaltic melt during xenolith ascent (e.g. Zinngrebe & Foley, 1995; Shaw & Klügel, 2002; Shaw *et al.*, 2006); (3) melting in the mantle prior to xenolith entrainment, induced by an infiltrating fluid (i.e. flux melting; e.g. Jones *et al.*, 1983; Ionov *et al.*, 1994; Demény *et al.*, 2004). However, most studies agree that that partial melting occurred very shortly before and/or during xenolith exhumation by the host magma. Thus a combination of metasomatically triggered melting followed and/or assisted by decompression melting during xenolith transport may be a realistic alternative in some cases (e.g. Dawson, 2002).

Recently, Ban *et al.* (2005) have shown, in a very detailed mass-balance study on glass-bearing xenoliths from the West Eifel, that the weight proportions of glass and the associated micro-phenocrysts match the composition of the preserved parent amphibole. We used the same approach and performed simple mass-balance calculations (least-squares fitting), to constrain the conclusions drawn from petrography, and to test which phase contributed, and to what extent, to the formation of the melt pockets. The results, reported in Table 8, show that in most cases amphibole-melting can account successfully for the melt pocket composition, and only a minor amount (<20%) of other phases (orthopyroxene and/or phlogopite) needs to be added to the reactant. Such a contribution of other phases agrees with textural observation (e.g. Fig. 4c showing Di_m growing on resorbed Opx_m), as well as with the conclusions of Ban *et al.* (2005), who stated that more Si-rich glass (i.e. >54 wt%) necessitates orthopyroxene contributing to the melt.

Trace element patterns of the bulk glass + micro-phenocryst pockets, calculated using the measured trace element abundances of glass and micro-phenocrysts and the respective mass-balance parameters (Table 8), are broadly identical to the measured amphibole composition (Fig. 18a and b). Higher LILE (Cs, Rb, Ba) concentrations in the calculated bulk melt patches in sample Ke 785* can be balanced by adding ~7 wt% of phlogopite (Fig. 18b), which is in line with mass balance (Table 8). The dominant control of amphibole to account for the trace element budget of the melt pockets is similar to results found in other suites of glass-bearing xenoliths (Chazot *et al.*, 1996*a*; Yaxley & Kamenetsky, 1999; Laurora *et al.*, 2001). Further, the obtained phase proportions for the melt pockets are in good agreement with the results from image analysis (Table 1). In addition, they are similar to the glass–cpx–ol proportions recorded in recent experiments on the

Table 8: Results of mass-balance calculations to test melt pocket formation by incongruent melting of the early metasomatic assemblages

Sample:*	1959/15	785	785	1965/25	1965/25	1965/3
Reactant						
amph	1·000	1·000	0·820	1·000	0·944	—
opx	—	—	0·078	—	0·056	0·406
phl	—	—	0·102	—	—	—
glass	—	—	—	—	—	0·594[1]
SiO_2	44·84	49·89	49·64	51·29	51·67	58·98
TiO_2	0·14	0·39	0·36	0·25	0·24	0·18
Cr_2O_3	2·32	2·91	2·58	1·27	1·21	0·09
Al_2O_3	13·68	7·62	7·69	8·00	7·57	9·61
$FeO_{(tot)}$	3·36	3·14	3·33	3·43	3·57	3·94
MnO	0·06	0·08	0·08	0·12	0·12	0·10
NiO	0·09	0·13	0·14	0·11	0·11	0·04
MgO	18·44	20·29	21·97	20·40	21·22	16·25
CaO	8·54	7·83	6·44	9·66	9·13	0·78
Na_2O	4·60	5·00	4·36	5·04	4·76	8·43
K_2O	0·49	0·32	0·96	0·42	0·40	0·60
Product						
glass	0·389	0·322	0·335	0·292	0·284	0·703[2]
ol	0·243	0·259	0·315	0·266	0·286	0·273
cpx	0·288	0·373	0·308	0·442	0·431	0·024
spl	0·052	0·032	0·028	—	—	—
carb	0·028	0·014	0·014	—	—	—
SiO_2	44·77	50·27	49·86	52·07	51·81	59·03
TiO_2	0·13	0·41	0·39	0·15	0·14	0·17
Cr_2O_3	2·13	3·14	2·72	1·09	1·06	0·15
Al_2O_3	13·64	7·64	7·70	7·98	7·76	9·57
$FeO_{(tot)}$	3·74	3·31	3·51	3·22	3·32	3·50
MnO	0·07	0·07	0·07	0·09	0·09	0·06
NiO	0·11	0·13	0·15	0·11	0·12	0·07
MgO	18·34	20·24	21·96	20·63	21·41	16·35
CaO	8·54	7·59	6·32	9·52	9·29	0·80
Na_2O	4·49	3·85	3·88	4·99	4·85	8·60
K_2O	0·60	0·96	1·00	0·15	0·14	0·91
Σr^2	**0·23**	**2·00**	**0·35**	**0·84**	**0·28**	**0·33**

*Prefix Ke omitted.
[1]Low-Si glass. [2]High-Si glass (see text for explanation).

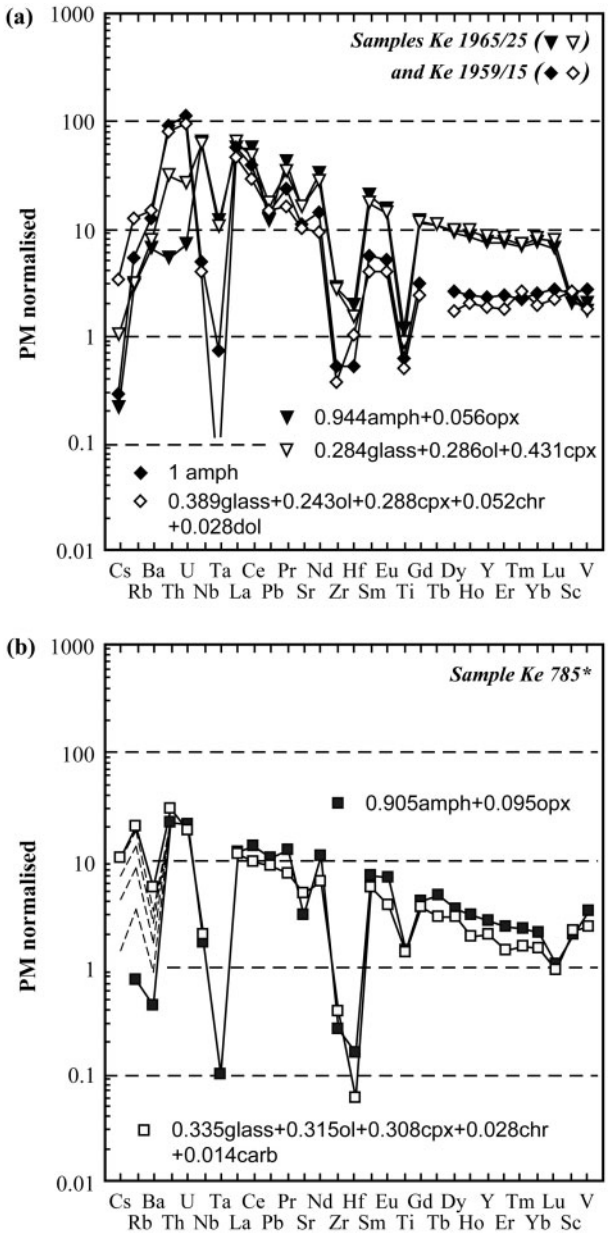

Fig. 18. Calculated trace element characteristics of reactants (in most cases amphibole + orthopyroxene; filled symbols) and products (melt pockets; open symbols) of the 'amphibole melting' model [see equation (1) in text]. The relative phase proportions were obtained by mass-balance calculations and are given in Table 8. The dashed lines in (b) show that the high LILE concentrations obtained for the product (bulk melt pocket) can be explained by adding about 7 wt% of phlogopite to the reactant (amphibole + orthopyroxene; Table 8). Further explanation is given in the text.

melting behaviour of amphibole in wehrlites at temperatures between 1175 and 1250°C and pressures of 0·5–1·0 GPa (Médard *et al.*, 2006). These temperatures are in good agreement with the estimates for the formation of olivine and chromite micro-phenocrysts in the melt pockets (Fig. 1b). The heat supply required for amphibole melting in the formerly low-T metasomatized Group III xenoliths ($\Delta T \sim 200$–300°C) may come from local heating shortly before or during xenolith entrainment in the host lava or from fluid infiltration that triggered melting (see discussion below).

Finally, formation of the most Si-enriched melt (adjacent to Opx_m in Group III-c samples) can be modelled assuming progressing interaction between infiltrating melt and orthopyroxene where the latter melts incongruently:

$$\text{opx} + \text{melt1} \rightarrow \text{ol} + \text{melt2} \pm \text{cpx} \quad (\text{see Table 8}). \qquad (1)$$

To calculate reaction (1) we chose the least evolved glass observed in melt patches in sample Ke 1965/3 (SiO_2 59·21 wt%; Mg-number 64·65) to represent the initial melt1, whereas melt2, adjacent to opx, is SiO_2-rich (65·30 wt%). Trace element abundances in glass next to orthopyroxene are shifted to lower concentrations (Table 6), which is in agreement with dilution caused by addition of a trace element-poor orthopyroxene component. The resultant phase proportions are similar to those observed at orthopyroxene–melt interfaces (i.e. high olivine and low cpx abundances), and are in agreement with experimental studies (Shaw *et al.*, 1998).

Partial melting triggered by fluid flux?

Mass-balance calculations provide an explanation for melt pocket formation by *in situ* partial melting. Thus, one might conclude that melting is simply the result of decompression and heating during xenolith transport in the host magma. However, there are two points that argue that melting was triggered by the infiltration of a fluid phase shortly before the xenoliths were sampled by the host magma: (1) the presence of occasionally high amounts of carbonate included in the melt pockets; (2) the extremely Na-rich clinopyroxene (Di_m) compositions, either included as micro-phenocrysts in the melt pocket or present as equilibrated grains around chromite in the single Type III-d xenolith (Fig. 3f). Both arguments will be discussed in the next section.

Formation of carbonates

Textures and compositions of carbonate globules can be explained by carbonate precipitation from a CO_2-bearing fluid. As demonstrated by several studies, high Ca/(Ca + Mg) values (Table 7) and low REE concentrations are strong arguments that the carbonates are cumulate crystals, precipitated from a CO_2-rich melt or a fluid and not quenched carbonated melts (Lee *et al.*, 2000; Ionov & Harmer, 2002). Oscillatory zoning (Fig. 5a and b) of individual carbonate crystals within single globules corroborates this interpretation. The rounded contacts toward glass (globules) are also in line with these findings. Similar globular forms were reported from experimental studies, and do not *a priori* imply the

presence of immiscible carbonate and silicate melts (e.g. Lee & Wyllie, 1996).

The high amount of carbonate in some melt pockets, however, (e.g. Fig. 4e) does need further explanation, as the incongruent melting reaction (1) does not account for the CO_2 required for carbonate precipitation during amphibole melting. Therefore, amphibole breakdown either occurred in an open system with addition of at least CO_2 (e.g. Laurora *et al.*, 2001; Ban *et al.*, 2005), or another pre-existing phase acted as a source of carbon. Oxidation of graphite, texturally identified as a part of the early assemblage (e.g. Fig. 3d), could account for some of the CO_2 necessary for carbonate formation. A change in fO_2 conditions is also indicated when the composition of glass-related spinel (Chr_m) and Ol_m are used for oxygen barometry, which yields oxygen fugacities well on the oxidized side of the carbon–carbonate–silicate buffer (Fig. 1b). However, increasing fO_2 triggered by closed-system decompression-induced melting alone does not appear feasible. Also, textures, such as straight contacts between graphite and Mg-calcite (Fig. 4c), suggest that carbonate grows on graphite (i.e. indicating local fO_2 conditions corresponding to carbon–carbonate equilibrium) rather than replacing it. We therefore interpret melt pocket formation to be triggered by the infiltration of a CO_2-rich fluid (i.e. flux melting; see also Ionov *et al.*, 1994). This interpretation also accounts for the presence of abundant vugs in the glass that could have contained a fluid (Ionov *et al.*, 1994, 2006), which was presumably lost during sample preparation. However, we emphasize here that late fluid infiltration had only subtle effects on the trace element composition of Type III-b and -c xenoliths.

Formation of Na-rich Cr diopside

Infiltration of CO_2-rich fluid would also explain the Na-rich composition of Di_m micro-phenocryst cores (Fig. 6a and b). Ionov *et al.* (2005) noted recently that clinopyroxenes in melt pockets are commonly characterized by Na_2O contents <1 wt%, mainly as a result of low cpx/melt partition coefficients at low pressures (e.g. Blundy *et al.*, 1995). Thus, very high Na_2O contents in Di_m micro-phenocrysts (Fig. 6a) suggest replacement of amphibole by Di_m and eventually Ol_m and Chr_m during reaction with a fluid at subsolidus conditions. An origin of micro-phenocrysts by replacement rather than crystallization from a melt is indicated by the identical crystallographic orientation of individual Di_m crystals in single melt pockets (Fig. 4a).

Once the solidus of the precursor phase(s) was reached (i.e. ~1050°C for amphibole; Niida & Green, 1999) silicate melt was generated *in situ* and led to the formation of clinopyroxene rims with lower Na contents (Fig. 6b) and the development of euhedral shapes in contact with melt (e.g. Fig. 4a and e). Eventual immiscibility between remaining fluid and newly formed melt (e.g. during xenolith ascent) would then explain the presence of carbonate globules and vugs enclosed in glass. Likewise, different origins of melt and carbonate were recently proposed for similar melt pockets from Hungarian xenoliths by Demény *et al.* (2004), who found oxygen isotope disequilibrium between carbonate globules and the host glass. Such a two-step model (fluid-induced replacement followed by melt generation) can be explained by CO_2-fluid infiltration occurring within the mantle at sub-solidus conditions, ultimately followed by xenolith entrainment in the host magma and transport to the surface. The host magma possibly supplied the additional heat necessary for melt generation. Fast decompression would further enhance melting and could also account for the lower Na contents in Di_m micro-phenocryst rims as a result of decreasing cpx/melt partition coefficients at decreasing pressures (Blundy *et al.*, 1995).

Rapid replacement of amphibole (± phlogopite) by an anhydrous phase assemblage indicates that the fluid was water-poor (e.g. low H_2O/CO_2 ratio; see Ionov *et al.*, 2006). This is corroborated by the fact that Mg-katophorite (presumably OH-rich; see above) is occasionally rimmed by a residual kaersutitic selvage (Fig. 4d). Such Ti-rich mantle amphiboles are commonly OH-poor as a result of partial dehydrogenation (e.g. Tiepolo *et al.*, 2001, and references therein).

Finally, the presence of the Type III-d xenolith, containing texturally equilibrated clinopyroxene of almost identical composition to Di_m micro-phenocrysts in melt pockets (Table 2; Figs 6a and 7b), further strengthens the argument that CO_2-fluid percolation started in the mantle before entrainment (i.e. enough time elapsed to allow this rock to anneal completely after the late metasomatic assemblage had formed). A similar conclusion can be drawn for the clearly host-related glass found in xenolith Ke 1959/27 (e.g. Fig. 13b). This Type III-c sample is characterized by the presence of Di_m micro-phenocrysts partly overgrown by mineral rims clearly related to the host basanite magma (kaersutite, Ti-augite and olivine with ~Fo88·5; Fig. 4f; Tables 3 and 4, and supplementary data at http://petrology.oxfordjournals.org). Kaersutite has major and trace element characteristics similar to typical basanitic and alkali basaltic amphibole phenocrysts (Fig. 9d). The special phase assemblages in this xenolith indicates that host-related basanitic melts intruded some Type III-c xenoliths and partly overprinted the assemblage formed slightly earlier by *in situ* derived alkali-rich peraluminous melts, fully preserved in other samples (e.g. Ke 1965/3 or Ke 785*).

ORIGIN OF METASOMATIZING AGENTS: TIMING AND TECTONIC SETTING

As noted above, late metasomatism was probably short-lived, started at mantle depths and probably continued

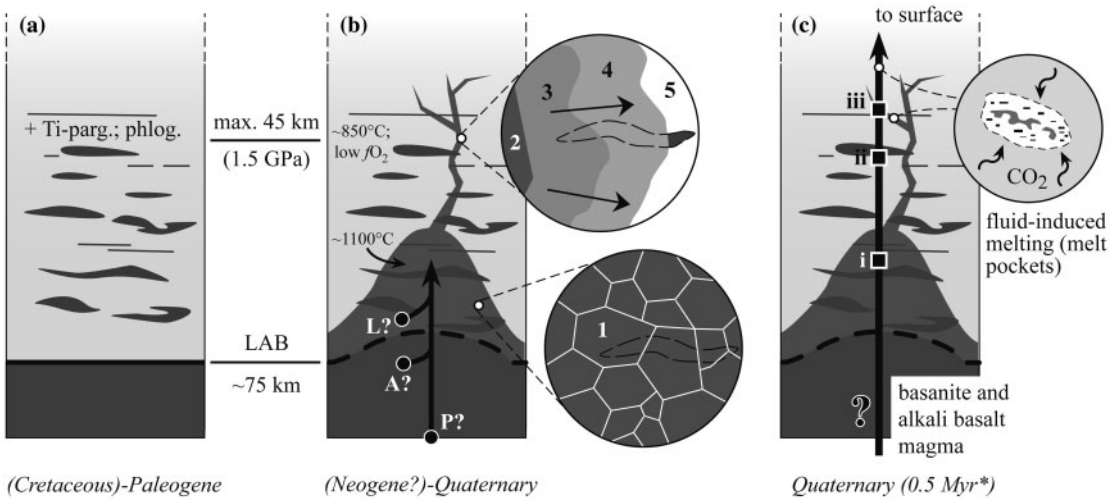

Fig. 19. Schematic illustration of the possible spatial and temporal relationships between the different metasomatic processes recorded by the investigated mantle xenoliths from Marsabit. (a) State of the lithosphere beneath Marsabit after Mesozoic rifting (decompression and cooling; Kaeser *et al.*, 2006). LAB, lithosphere–asthenosphere boundary (Henjes-Kunst & Altherr, 1992). Penetrative deformation is indicated by fine horizontal lines. Dark grey boudins indicate compositional heterogeneities including deformed pyroxenite bands and cpx-rich lherzolite (Group I xenoliths), including associated Ti-pargasite and phlogopite. (b) Schematic representation of the EARS-related heating as a result of mafic silicate melt impregnation (Kaeser *et al.*, 2006; bold arrow), and propagation (and associated melt–rock reaction) of residual volatile Si-rich melts in colder and relatively reduced lithospheric domains (early metasomatism; this study). L?, A?, and P? represent possible, yet unconstrained, components in the initial melt, either deriving from the lower lithosphere, the asthenosphere or a mantle plume, respectively. Close-ups: 1, possible location of statically recrystallized silicate melt metasomatized Group II lherzolite (Kaeser *et al.*, 2006); 2, SiO_2–Na_2O–CO_2–H_2O-rich melt responsible for metasomatism in Group III peridotites; 3, position of Type III-c amphibole-harzburgite and dunite (close to the metasomatizing agent); 4, position of Type III-b harzburgite; 5, position of Type III-a harzburgite (least metasomatized). Percolation through and/or reaction with pre-existing heterogeneities (dashed lines) may account for several trace element characteristics (see text). Small arrows indicate melt or fluid percolation away from the initial source (e.g. a melt conduit). (c) Sampling of the xenoliths by Quaternary basanites and alkali basalts (*Brotzu *et al.*, 1984); i, Group II (grt)-spinel lherzolites; ii, non-metasomatized Group I (grt)-spinel lherzolites; iii, strongly metasomatized Type III-a to -d harzburgites and dunites. Close-up: melt pocket formation during this late-stage event triggered by CO_2-rich fluid. It should be noted that the vertical differences are hypothetical owing to the lack of accurate constraints on the sampling depth. The relationship between Group II and III could also be lateral (e.g. away from a larger melt conduit).

during xenolith transport in the host magma. The relation between fluid infiltration and xenolith entrainment suggests that the source of the fluid is intimately related to the host magma. Volatile components such as CO_2 play a major role during wall-rock disruption and xenolith sampling at depth (e.g. Spera, 1984; Lensky *et al.*, 2006). Thus the CO_2-rich fluids may be derived directly from the rising basanitic magma that ultimately sampled the xenoliths (Fig. 19). Alternatively, the CO_2-fluid may be derived from decarbonation reactions (CO_2 release) at greater depths where rising carbonate-rich melts reach the solidus of carbonated lherzolite (see Fig. 2 and Lee & Wyllie, 2000, and references therein). Finally, we would like to stress that silicate melt (now glass) was formed *in situ*, within the xenoliths and, thus, does not represent an extraneously derived metasomatizing agent.

In contrast to the melt pockets, the age of formation of the early metasomatic assemblages is more difficult to assess. Relative age information can be obtained from textural relationships. Metasomatism partly overprints the strongly deformed fabric of the pre-metasomatic Group III rocks. Because pervasive deformation probably occurred during the development of the Mesozoic Anza Graben (Kaeser *et al.*, 2006; Fig. 1), metasomatism should be younger. In the geodynamic context of Marsabit, this would then most probably be in association with the young (Miocene–Pleistocene) magmatic activity of the Kenya Rift (EARS).

The occurrence of orthopyroxene-saturated volatile-rich melts in a region characterized by voluminous alkaline magmatism is enigmatic, however. It seems most plausible that such melts evolved from alkaline mafic melts through melt–rock reaction, as in the models of Bedini *et al.* (1997) or Bodinier *et al.* (2004). In their study, Bedini *et al.* (1997) explained metasomatism in the enriched and deformed harzburgite xenoliths from southern Ethiopia (~200 km north of Marsabit) by complex reactive porous flow processes, starting with an 'ordinary' ocean island basalt type mafic silicate melt. Their hypothetical melts in equilibrium with the metasomatized xenoliths have trace element compositions strikingly similar to the calculated silicate melts in equilibrium with euhedral Mg-katophorite (Fig. 17). In Marsabit, the heated (1000–1200°C) and recrystallized Group II lherzolites provide evidence for recent, EARS-related metasomatism through alkaline mafic melts, possibly parental to the basanites extruded at the

surface (Kaeser *et al.*, 2006). Similar to the process invoked for the Ethiopian xenoliths, continuous melt–rock reaction and fractionation could have led to the formation of small fractions of highly evolved melts infiltrating and metasomatizing the cold and deformed uppermost mantle represented by Group III harzburgites (Fig. 19; see also Ionov *et al.*, 2006, for a similar model). A relationship between metasomatism in Group II and III peridotites is supported by several xenoliths showing transitional textures and trace element signatures (i.e. strong U–Th–LREE enrichment in some Group II clinopyroxenes; Kaeser *et al.*, 2006).

Alternatively, Si- and volatile-enriched melts may be residual liquids from the crystallization of alkali basaltic or basanitic veins (i.e. hornblendite or clinopyroxenite), ultimately metasomatizing the adjacent peridotitic wall-rock (e.g. Harte *et al.*, 1993; Wulff-Pedersen *et al.*, 1999; Bodinier *et al.*, 2004). This remains speculative, however, as such veins or dykes have not yet been reported from Marsabit. It can thus not be resolved whether early metasomatism reflects a large, kilometre-scale process (e.g. an upwelling melt percolation front as proposed for the mantle beneath southern Ethiopia; Bedini *et al.*, 1997), or whether metasomatism is restricted to narrower zones adjacent to small (centimetre- to metre-scale) melt conduits (e.g. wall-rock metasomatism).

Extensive melt–rock reaction in the mantle beneath the EARS, however, is indicated by numerous xenolith suites containing abundant and variably metasomatized rocks (e.g. Tanzania: Dawson & Smith, 1988; Rudnick *et al.*, 1993; Lee & Rudnick, 1999; Dawson, 2002, and references therein; Ethiopia: Bedini *et al.*, 1997; Rooney *et al.*, 2005). In the case of northern Kenya, seismic studies point to a broad zone of low seismic wave velocities in the relatively shallow mantle ~600 km across and reaching depths of <40 km depth beneath Lake Turkana and ~90 km beneath Marsabit (see Simiyu & Keller, 1997). This anomaly is commonly interpreted as a zone of hot rising mantle containing small amounts (3–5%) of melt (Green *et al.*, 1991). Upwelling of such melts into the lithospheric mantle followed by reaction could thus account for the metasomatism seen in the Marsabit mantle xenoliths. Such interaction of sub-lithospheric melts or fluids (asthenospheric or plume-related) with colder lithospheric material is one of the major processes invoked to account for the heterogeneous isotopic composition of primitive lavas from numerous parts of the EARS (e.g. Macdonald *et al.*, 2001; Furman *et al.*, 2006, and references therein).

ACKNOWLEDGEMENTS

We would like to thank Edwin Gnos and Alfons Berger (Bern), and Hans-Peter Meyer (Heidelberg) for assistance with microprobe work, as well as André Villard, who provided top-quality thin sections. Discussion with Othmar Müntener, Arjan Dijkstra, Rainer Altherr, Jean-Louis Bodinier and Alan Woodland helped to clarify many aspects of this work. We thank Hilary Downes, Tanya Furman and Dmitri Ionov for constructive reviews, and Marjorie Wilson for valuable comments and editorial handling. This publication is part of a project financed by the Swiss National Science Foundation (grant No. 200021-100647/1 to A.K.). Further financial support from the SNF (grants 21-26579.89 and 200021-103479/1) for the electron microprobe facility at the Institute of Geological Sciences, University of Bern, is acknowledged.

SUPPLEMENTARY DATA

Supplementary data for this paper are available at *Journal of Petrology* online.

REFERENCES

Adam, J. & Green, T. (2001). Experimentally determined partition coefficients for minor and trace elements in peridotite minerals and carbonatitic melt, and their relevance to natural carbonatites. *European Journal of Mineralogy* **13**, 815–827.

Adam, J., Green, T. H., Sie, S. H. & Ryan, C. G. (1997). Trace element partitioning between aqueous fluids, silicate melts and minerals. *European Journal of Mineralogy* **9**, 569–584.

Bailey, D. K. (1987). Mantle metasomatism - perspective and prospect. In: Fitton, J. G. & Upton, B. G. J. (eds) *Alkaline Igneous Rocks*. London: Geological Society, Special Publications No. **30**, 1–13.

Baker, B. H., Williams, L. A. J., Miller, J. A. & Fitch, F. J. (1971). Sequence and geochronology of the Kenya rift volcanics. *Tectonophysics* **11**, 191–215.

Bali, E., Szabó, C., Vaselli, O. & Török, K. (2002). Significance of silicate melt pockets in upper mantle xenoliths from the Bakony–Balaton highland volcanic field, Western Hungary. *Lithos* **61**, 79–102.

Ballhaus, C., Berry, R. F. & Green, D. H. (1991). High pressure experimental calibration of the olivine–orthopyroxene–spinel oxygen geobarometer: implications for the oxidation state of the upper mantle. *Contributions to Mineralogy and Petrology* **107**, 27–40.

Ban, M., Witt-Eickschen, G., Klein, M. & Seck, H. A. (2005). The origin of glasses in hydrous mantle xenoliths from the West Eifel, Germany: incongruent break down of amphibole. *Contributions to Mineralogy and Petrology* **148**, 511–523.

Barclay, J. & Carmichael, I. S. E. (2004). A hornblende basalt from western Mexico: water-saturated phase relations constrain a pressure–temperature window of eruptibility. *Journal of Petrology* **45**, 485–506.

Bedini, R. M., Bodinier, J.-L., Dautria, J.-M. & Morten, L. (1997). Evolution of LILE-enriched small melt fractions in the lithospheric mantle: a case study from the East African Rift. *Earth and Planetary Science Letters* **153**, 67–83.

Blundy, J., Falloon, T. J., Wood, B. J. & Dalton, J. A. (1995). Sodium partitioning between clinopyroxene and silicate melts. *Journal of Geophysical Research* **100**, 15501–15515.

Bodinier, J. L., Merlet, C., Bedini, R. M., Simien, F., Remaidi, M. & Garrido, C. J. (1996). Distribution of niobium, tantalum, and other highly incompatible trace elements in the lithospheric mantle: the spinel paradox. *Geochimica et Cosmochimica Acta* **60**, 545–550.

Bodinier, J.-L., Menzies, M. A., Shimizu, N., Frey, F. A. & McPherson, E. (2004). Silicate, hydrous and carbonate

metasomatism at Lherz, France: contemporaneous derivates of silicate melt–harzburgite reaction. *Journal of Petrology* **45**, 299–320.

Brey, G. P. & Köhler, T. (1990). Geothermobarometry in four-phase lherzolites II. New thermobarometers, and practical assessment of existing thermobarometers. *Journal of Petrology* **31**, 1353–1378.

Brotzu, P., Morbideli, L., Nicoletti, M., Piccirillo, E. M. & Traversa, G. (1984). Miocene to Quaternary volcanism in eastern Africa: sequence and chronology. *Tectonophysics* **101**, 75–86.

Chazot, G., Menzies, M. A. & Harte, B. (1996*a*). Determination of partition coefficients between apatite, clinopyroxene, amphibole, and melt in natural spinel lherzolites from Yemen: implications for wet melting of the lithospheric mantle. *Geochimica et Cosmochimica Acta* **60**, 423–437.

Chazot, G., Menzies, M. A. & Harte, B. (1996*b*). Silicate glasses in spinel lherzolites from Yemen: origin and chemical composition. *Chemical Geology* **134**, 159–179.

Coltorti, M., Bonadiman, C., Hinton, R. W., Siena, F. & Upton, B. G. J. (1999). Carbonatite metasomatism of the oceanic upper mantle: evidence from clinopyroxenes and glasses in ultramafic xenoliths of Grande Comore, Indian Ocean. *Journal of Petrology* **40**, 133–165.

Coltorti, M., Beccaluva, L., Bonadiman, C., Salvini, L. & Siena, F. (2000). Glasses in mantle xenoliths as geochemical indicators of metasomatic agents. *Earth and Planetary Science Letters* **183**, 303–320.

Costa, F., Dungan, M. A. & Singer, B. S. (2001). Magmatic Na-rich phlogopite in a suite of gabbroic crustal xenoliths from Volcán San Pedro, Chilean Andes: evidence for a solvus relation between phlogopite and aspidolite. *American Mineralogist* **86**, 29–35.

Dautria, J.-M., Dupuy, C., Takherist, D. & Dostal, J. (1992). Carbonate metasomatism in the lithospheric mantle: peridotitic xenoliths from a melilitic district of the Sahara basin. *Contributions to Mineralogy and Petrology* **111**, 37–52.

Dawson, J. B. (2002). Metasomatism and partial melting in upper-mantle peridotite xenoliths from the Lashaine volcano, Northern Tanzania. *Journal of Petrology* **43**, 1749–1777.

Dawson, J. B. & Smith, J. V. (1988). Metasomatized and veined upper mantle xenoliths from Pello Hill, Tanzania: evidence for anomalously light mantle beneath the Tanzanian sector of the East African rift valley. *Contributions to Mineralogy and Petrology* **100**, 510–527.

Demény, A., Vennemann, T. W., Hegner, E., Nagy, G., Milton, J. A., Embey-Isztin, A., Homonnay, Z. & Dobosi, G. (2004). Trace element and C–O–Sr–Nd isotope evidence for subduction related carbonate–silicate melts in mantle xenoliths (Pannonian Basin, Hungary). *Lithos* **75**, 89–113.

Draper, D. S. & Green, T. H. (1997). *P–T* phase relations of silicic, alkaline, aluminous mantle-xenolith glasses under anhydrous and C–O–H fluid-saturated conditions. *Journal of Petrology* **38**, 1187–1224.

Eggler, D. H. & Baker, D. R. (1982). Reduced volatiles in the system C–O–H: implications to mantle melting, fluid formation and diamond genesis. In: Akimoto, S. & Manghnani, M. H. (eds) *High Pressure Research in Geophysics*. Tokyo: Center for Academic Publications Japan, pp. 237–250.

Ferraris, C., Grobéty, B., Früh-Green, G. L. & Wessicken, R. (2004). Intergrowth of graphite within phlogopite from Finero ultramafic complex (Italian Western Alps): implications for mantle crystallization of primary-texture mica. *European Journal of Mineralogy* **16**, 899–908.

Francis, D. M. (1976). Amphibole pyroxenite xenoliths: cumulate or replacement phenomena from the upper mantle, Nunivak Island, Alaska. *Contributions to Mineralogy and Petrology* **58**, 51–61.

Frey, F. A. & Green, D. H. (1974). Mineralogy, geochemistry and origin of lherzolite inclusions in Victorian basanites. *Geochimica et Cosmochimica Acta* **38**, 1023–1059.

Frost, D. J. & Wood, B. J. (1998). The fugacity of carbon dioxide and the graphite/diamond CO equilibrium between 35 and 77 kbar at 925 to 1650°C. (vol 61, pg 1565, 1997). *Geochimica et Cosmochimica Acta* **62**, 725–725.

Fumagalli, P. & Poli, S. (2005). Experimentally determined phase relations in hydrous peridotites to 6·5 GPa and their consequences on the dynamics of subduction zones. *Journal of Petrology* **46**, 555–578.

Furman, T., Kaleta, K. M., Bryce, J. G. & Hanan, B. B. (2006). Tertiary mafic lavas of Turkana, Kenya: constraints on East African plume structure and the occurrence of high-mu volcanism in Africa. *Journal of Petrology* **47**, 1221–1244.

Gasparik, T. (1987). Orthopyroxene thermobarometry in simple and complex systems. *Contributions to Mineralogy and Petrology* **96**, 357–370.

Godard, M., Bodinier, J.-L. & Vasseur, G. (1995). Effects of mineralogical reactions on trace element redistributions in mantle rocks during percolation processes: a chromatographic approach. *Earth and Planetary Science Letters* **133**, 449–461.

Green, D. H. & Wallace, M. E. (1988). Mantle metasomatism by ephemeral carbonatite melts. *Nature* **336**, 459–462.

Green, W. V., Achauer, U. & Meyer, R. P. (1991). A 3-dimensional seismic image of the crust and upper mantle beneath the Kenya rift. *Nature* **354**, 199–203.

Grégoire, M., McInnes, B. I. A. & O'Reilly, S. Y. (2001). Hydrous metasomatism of oceanic sub-arc mantle, Lihir, Papua New Guinea, Part 2. Trace element characteristics of slab-derived fluids. *Lithos* **59**, 91–108.

Grégoire, M., Bell, D. R. & Le Roex, A. P. (2002). Trace element geochemistry of phlogopite-rich mafic mantle xenoliths: their classification and their relationship to phlogopite-bearing peridotites and kimberlites. *Contributions to Mineralogy and Petrology* **142**, 603–625.

Grove, T. L., Chatterjee, N., Parman, S. W. & Médard, E. (2006). The influence of H_2O on mantle wedge melting. *Earth and Planetary Science Letters* **249**, 74–89.

Harte, B., Hunter, R. H. & Kinny, P. D. (1993). Melt geometry, movement and crystallization, in relation to mantle dykes, veins and metasomatism. *Philosophical Transactions of the Royal Society of London Series A* **342**, 1–21.

Hauri, E. H., Shimizu, N., Dieu, J. J. & Hart, S. R. (1993). Evidence for hotspot-related carbonatite metasomatism in the oceanic upper mantle. *Nature* **365**, 221–227.

Henjes-Kunst, F. & Altherr, R. (1992). Metamorphic petrology of xenoliths from Kenya and northern Tanzania and implications for geotherms and lithospheric structures. *Journal of Petrology* **33**, 1125–1156.

Ionov, D. A. (1998). Trace element composition of mantle-derived carbonates and coexisting phases in peridotite xenoliths from alkali basalts. *Journal of Petrology* **39**, 1931–1941.

Ionov, D. A. & Harmer, R. E. (2002). Trace element distribution in calcite–dolomite carbonatites from Spitskop: inferences for differentiation of carbonatite magmas and the origin of carbonates in mantle xenoliths. *Earth and Planetary Science Letters* **198**, 495–510.

Ionov, D. A. & Hofmann, A. W. (1995). Nb–Ta-rich mantle amphiboles and micas—implications for subduction-related metasomatic trace-element fractionations. *Earth and Planetary Science Letters* **131**, 341–356.

Ionov, D. A., Dupuy, C., O'Reilly, S. Y., Kopylova, M. G. & Genshaft, Y. S. (1993). Carbonated peridotite xenoliths from Spitsbergen: implications for trace element signature of mantle

carbonate metasomatism. *Earth and Planetary Science Letters* **119**, 283–297.

Ionov, D. A., Hofmann, A. W. & Shimizu, N. (1994). Metasomatism-induced melting in mantle xenoliths from Mongolia. *Journal of Petrology* **35**, 753–785.

Ionov, D. A., O'Reilly, S. Y., Genshaft, Y. S. & Kopylova, M. G. (1996). Carbonate-bearing mantle peridotite xenoliths from Spitsbergen: phase relationship, mineral compositions and trace-element residence. *Contributions to Mineralogy and Petrology* **125**, 375–392.

Ionov, D. A., Griffin, W. L. & O'Reilly, S. Y. (1997). Volatile-bearing minerals and lithophile trace elements in the upper mantle. *Chemical Geology* **141**, 153–184.

Ionov, D. A., Bodinier, J.-L., Mukasa, S. B. & Zanetti, A. (2002). Mechanisms and sources of mantle metasomatism: major and trace element compositions of peridotite xenoliths from Spitsbergen in the context of numerical modelling. *Journal of Petrology* **43**, 2219–2259.

Ionov, D. A., Prikhodko, V. S., Bodinier, J. L., Sobolev, A. V. & Weis, D. (2005). Lithospheric mantle beneath the south-eastern Siberian craton: petrology of peridotite xenoliths in basalts from the Tokinsky Stanovik. *Contributions to Mineralogy and Petrology* **149**, 647–665.

Ionov, D. A., Chazot, G., Chauvel, C., Merlet, C. & Bodinier, J. L. (2006). Trace element distribution in peridotite xenoliths from Tok, SE Siberian craton: a record of pervasive, multi-stage metasomatism in shallow refractory mantle. *Geochimica et Cosmochimica Acta* **70**, 1231–1260.

Jones, A. P., Smith, J. V. & Dawson, J. B. (1983). Glasses in mantle xenoliths from Olmani, Tanzania. *Journal of Geology* **91**, 167–178.

Kaeser, B. (2006). Mantle xenoliths from the Marsabit volcanic field: a case study on the evolution of the lithospheric mantle in a continental rift environment. Ph.D. thesis, University of Neuchâtel, 207 pp.

Kaeser, B., Kalt, A. & Pettke, T. (2006). Evolution of the lithospheric mantle beneath the Marsabit volcanic field (northern Kenya): constraints from textural, P–T and geochemical studies on xenoliths. *Journal of Petrology* **47**, 2149–2184.

Kelemen, P. B., Whitehead, J. A., Aharonov, E. & Jordahl, K. A. (1995). Experiments on flow focusing in soluble porous media, with applications to melt extraction from the mantle. *Journal of Geophysical Research* **100**, 475–496.

Kessel, R., Ulmer, P., Pettke, T., Schmidt, M. W. & Thompson, A. B. (2005). The water–basalt system at 4 to 6 GPa: phase relations and second critical endpoint in a K-free eclogite at 700 to 1400°C. *Earth and Planetary Science Letters* **237**, 873–892.

Key, R. M., Rop, B. P. & Rundle, C. C. (1987). The development of the late Cenozoic alkali basaltic Marsabit shield volcano, northern Kenya. *Journal of African Earth Sciences* **6**, 475–491.

King, B. C. (1970). Vulcanicity and rift tectonics in east Africa. In: Clifford, T. N. & Gass, I. G. (eds) *African Magmatism and Tectonics*. Edinburgh: Oliver & Boyd, pp. 263–285.

Klemme, S. & O'Neill, H. S. (2000). The near-solidus transition from garnet lherzolite to spinel lherzolite. *Contributions to Mineralogy and Petrology* **138**, 237–248.

LaTourrette, T., Hervig, R. L. & Holloway, J. R. (1995). Trace-element partitioning between amphibole, phlogopite, and basanite melt. *Earth and Planetary Science Letters* **135**, 13–30.

Laurora, A., Mazzucchelli, M., Rivalenti, G., Vannucci, R., Zanetti, A., Barbieri, M. A. & Cingolani, C. A. (2001). Metasomatism and melting in carbonated peridotite xenoliths from the mantle wedge: the Gobernador Gregores case (southern Patagonia). *Journal of Petrology* **42**, 69–87.

Leake, B. E., Woolley, A. R., Arps, C. E. S., *et al.* (1997). Nomenclature of amphiboles: report of the subcommittee on amphiboles of the International Mineralogical Association, commission on new minerals and mineral names. *American Mineralogist* **82**, 1019–1037.

Lee, C.-T. & Rudnick, R. (1999). Compositionally stratified cratonic lithosphere; petrology and geochemistry of peridotite xenoliths from the Labait Volcano, Tanzanie. In: Gurney, J., Gurney, J. L., Pascoe, M. D. & Richardson, S. H. (eds) *Proceedings of the 7th international Kimberlite Conference*. Cape Town: Red Roof Design, 503–521.

Lee, C.-T., Rudnick, R. L., McDonough, W. F. & Horn, I. (2000). Petrologic and geochemical investigation of carbonates in peridotite xenoliths from northeastern Tanzania. *Contributions to Mineralogy and Petrology* **139**, 470–484.

Lee, W. J. & Wyllie, P. J. (1996). Liquid immiscibility in the join $NaAlSi_3O_8$–$CaCO_3$ to 2·5 GPa and the origin of calciocarbonatite magmas. *Journal of Petrology* **37**, 1125–1152.

Lee, W. J. & Wyllie, P. J. (2000). The system CaO–MgO–SiO_2–CO_2 at 1 GPa, metasomatic wehrlites, and primary carbonatite magmas. *Contributions to Mineralogy and Petrology* **138**, 214–228.

Lensky, N. G., Niebo, R. W., Holloway, J. R., Lyakhovsky, V. & Navon, O. (2006). Bubble nucleation as a trigger for xenolith entrapment in mantle melts. *Earth and Planetary Science Letters* **245**, 278–288.

Luth, R. W. (2003). Mantle volatiles—distribution and consequences. In: Holland, H. D. & Turekian, K. K. (eds) *Treatise on Geochemistry*. Amsterdam: Elsevier, pp. 319–361.

Maaløe, S. & Printzlau, I. (1979). Natural partial melting of spinel lherzolite. *Journal of Petrology* **20**, 727–741.

Macdonald, R., Rogers, N. W., Fitton, J. G., Black, S. & Smith, M. (2001). Plume–lithosphere interactions in the generation of the basalts of the Kenya Rift, East Africa. *Journal of Petrology* **42**, 877–900.

Manning, C. E. (2004). The chemistry of subduction-zone fluids. *Earth and Planetary Science Letters* **223**, 1–16.

Maury, R. C., Defant, M. J. & Joron, J. L. (1992). Metasomatism of the sub-arc mantle inferred from trace-elements in Philippine xenoliths. *Nature* **360**, 661–663.

McDonough, W. F. & Sun, S. S. (1995). The composition of the Earth. *Chemical Geology* **120**, 223–253.

McInnes, B. I. A., Grégoire, M., Binns, R. A., Herzig, P. M. & Hannington, M. D. (2001). Hydrous metasomatism of oceanic sub-arc mantle, Lihir, Papua New Guinea: petrology and geochemistry of fluid-metasomatised mantle wedge xenoliths. *Earth and Planetary Science Letters* **188**, 169–183.

Médard, E., Schmidt, M. W., Schiano, P. & Ottolini, L. (2006). Melting of amphibole-bearing wehrlites: an experimental study on the origin of ultra-calcic nepheline-normative melts. *Journal of Petrology* **47**, 481–504.

Meert, J. G. (2003). A synopsis of events related to the assembly of eastern Gondwana. *Tectonophysics* **362**, 1–40.

Menzies, M. A. & Hawkesworth, C. J. (1987). *Mantle Metsomatism*. London: Academic Press.

Moine, B. N., Grégoire, M., O'Reilly, S. Y., Sheppard, S. M. F. & Cottin, J. Y. (2001). High field strength element fractionation in the upper mantle: evidence from amphibole-rich composite mantle xenoliths from the Kerguelen Islands (Indian Ocean). *Journal of Petrology* **42**, 2145–2167.

Moine, B. N., Grégoire, M., O'Reilly, S. Y., Delpech, G., Sheppard, S. M. F., Lorand, J. P., Renac, C., Giret, A. & Cottin, J. Y. (2004). Carbonatite melt in the upper mantle beneath the Kerguelen Archipelago. *Lithos* **75**, 239–252.

Morishita, T., Arai, S. & Green, D. H. (2003). Evolution of low-Al orthopyroxene in the Horoman peridotite, Japan: an unusual indicator of metasomatizing fluids. *Journal of Petrology* **44**, 1237–1246.

Morley, C. K. (1999). Tectonic evolution of the East African Rift System and the modifying influence of magmatism: a review. *Acta Vulcanologica* **11**, 1–19.

Navon, O. & Stolper, E. (1987). Geochemical consequences of melt percolation: the upper mantle as a chromatographic column. *Journal of Geology* **95**, 285–307.

Neumann, E.-R. & Wulff-Pedersen, E. (1997). The origin of highly silicic glass in mantle xenoliths from the Canary Islands. *Journal of Petrology* **38**, 1513–1539.

Neumann, E.-R., Wulff-Pedersen, E., Pearson, N. J. & Spencer, E. A. (2002). Mantle xenoliths from Tenerife (Canary Islands): evidence for reactions between mantle peridotites and silicic carbonatite melts inducing Ca metasomatism. *Journal of Petrology* **43**, 825–857.

Niida, K. & Green, D. H. (1999). Stability and chemical composition of pargasitic amphibole in MORB pyrolite under upper mantle conditions. *Contributions to Mineralogy and Petrology* **135**, 18–40.

Norman, M. D. (1998). Melting and metasomatism in the continental lithosphere: laser ablation ICPMS analysis of minerals in spinel lherzolites from eastern Australia. *Contributions to Mineralogy and Petrology* **130**, 240–255.

Odling, N. W. A. (1994). An experimental simulation of upper-mantle metasomatism. *American Mineralogist* **79**, 148–153.

Olker, B. (2001). Entwicklung und Anwendung eines Computerprogrammes zur numerischen Modellierung von Diffusionsprofilen in Mineralkörnern. Ph.D. thesis, University of Heidelberg, 269 pp.

O'Neill, H. S. (1987). Quartz–fayalite–iron and quartz–fayalite–magnetite equilibria and the free-energy of formation of fayalite (Fe_2SiO_4) and magnetite (Fe_3O_4). *American Mineralogist* **72**, 67–75.

O'Reilly, S. Y. & Griffin, W. L. (2000). Apatite in the mantle: implications for metasomatic processes and high heat production in Phanerozoic mantle. *Lithos* **53**, 217–232.

Parkinson, I. J., Arculus, R. J. & Eggins, S. M. (2003). Peridotite xenoliths from Grenada, Lesser Antilles island arc. *Contributions to Mineralogy and Petrology* **146**, 241–262.

Pearson, D. G., Boyd, F. R., Haggerty, S. E., Pasteris, J. D., Field, S. W., Nixon, P. H. & Pokhilenko, N. P. (1994). The characterization and origin of graphite in cratonic lithospheric mantle—a petrological carbon-isotope and Raman-spectroscopic study. *Contributions to Mineralogy and Petrology* **115**, 449–466.

Pearson, D. G., Canil, D. & Shirey, S. B. (2003). Mantle samples included in volcanic rocks: xenoliths and diamonds. In: Carlson, R. W. (ed.) *Treatise on Geochemistry*. Amsterdam: Elsevier, pp. 171–275.

Pettke, T., Halter, W. E., Webster, J. D., Aigner-Torres, M. & Heinrich, C. A. (2004). Accurate quantification of melt inclusion chemistry by LA-ICPMS: a comparison with EMP and SIMS and the adventages and possible limitations of these methods. *Lithos* **78**, 333–361.

Popp, R. K., Virgo, D. & Phillips, M. W. (1995). H deficiency in kaersutitic amphiboles: experimental verification. *American Mineralogist* **80**, 1347–1350.

Powell, W., Zhang, M., O'Reilly, S. Y. & Tiepolo, M. (2004). Mantle amphibole trace-element and isotope signatures trace multiple metasomatic episodes in lithospheric mantle, western Victoria, Australia. *Lithos* **75**, 141–171.

Prouteau, G. & Scaillet, B. (2003). Experimental constraints on the origin of the 1991 Pinatubo dacite. *Journal of Petrology* **44**, 2203–2241.

Rampone, E., Bottazzi, P. & Ottolini, L. (1991). Complementary Ti and Zr anomalies in orthopyroxene and clinopyroxene from mantle peridotites. *Nature* **354**, 518–520.

Rapp, R. P. (1995). Amphibole-out phase-boundary in partially melted metabasalt, its control over liquid fraction and composition, and source permeability. *Journal of Geophysical Research—Solid Earth* **100**, 15601–15610.

Rivalenti, G., Zanetti, A., Mazzucchelli, M., Vannucci, R. & Cingolani, C. A. (2004). Equivocal carbonatite markers in the mantle xenoliths of the Patagonia backarc: the Gobernador Gregores case (Santa Cruz Province, Argentina). *Contributions to Mineralogy and Petrology* **147**, 647–670.

Rooney, T. O., Furman, T., Yirgu, G. & Ayalew, D. (2005). Structure of the Ethiopian lithosphere: xenolith evidence in the Main Ethiopian Rift. *Geochimica et Cosmochimica Acta* **69**, 3889–3910.

Rudnick, R. L., McDonough, W. F. & Chappell, B. W. (1993). Carbonatite metasomatism in the northern Tanzanian mantle: petrographic and geochemical characteristics. *Earth and Planetary Science Letters* **114**, 463–475.

Rudnick, R. L., Ireland, T. R., Gehrels, G., Irving, A. J., Chesley, J. T. & Hanchar, J. M. (1999). Dating mantle metasomatism: U–Pb geochronology of zircons in cratonic mantle xenoliths from Montana and Tanzania. In: Gurney, J., Gurney, J. L., Pascoe, M. D. & Richardson, S. H. (eds) *Proceedings of the 7th international Kimberlite Conference*. Cape Town: Red Roof Design, pp. 728–735.

Shaw, C. S. J. & Eyzaguirre, J. (2000). Origin of megacrysts in the mafic alkaline lavas of the West Eifel volcanic field, Germany. *Lithos* **50**, 75–95.

Shaw, C. S. & Klügel, A. (2002). The pressure and temperature conditions and timing of glass formation in mantle-derived xenoliths from Baarley, West Eifel, Germany: the case for amphibole breakdown, lava infiltration and mineral–melt reaction. *Mineralogy and Petrology* **74**, 163–187.

Shaw, C. S., Thibault, Y., Edgar, A. D. & Lloyd, F. E. (1998). Mechanism of orthopyroxene dissolution in silica-undersaturated melts at 1 atmosphere and implications for the origin of silica-rich glass in mantle xenoliths. *Contributions to Mineralogy and Petrology* **132**, 354–370.

Shaw, S. J., Heidelbach, F. & Dingwell, D. B. (2006). The origin of reaction textures in mantle peridotite xenoliths from Sal Island, Cape Verde: the case for 'metasomatism' by the host lava. *Contributions to Mineralogy and Petrology* **151**, 681–697.

Simiyu, S. M. & Keller, G. R. (1997). An integrated analysis of lithospheric structure across the East African plateau based on gravity anomalies and recent seismic studies. *Tectonophysics* **278**, 291–313.

Smith, D. (1999). Temperatures and pressures of mineral equilibration in peridotite xenoliths: review, discussion, and implications. In: Fei, Y., Bertka, C. M. & Mysen, B. O. (eds) *Mantle Petrology: Field Observation and High-Pressure Experimentation. A Tribute to Francis R. (Joe) Boyd. Geochemical Society Special Publications* **6**, 171–188.

Smith, D., Riter, J. C. A. & Mertzman, S. A. (1999). Water–rock interactions, orthopyroxene growth, and Si-enrichment in the mantle: evidence in xenoliths from the Colorado Plateau, southwestern United States (vol 165, pg 45, 1999). *Earth and Planetary Science Letters* **167**, 347–356.

Spera, F. J. (1984). Carbon dioxide in petrogenesis 3. Role of volatiles in the ascent of alkaline magma with special reference to xenolith-bearing mafic lavas. *Contributions to Mineralogy and Petrology* **88**, 217–232.

Tiepolo, M., Bottazzi, P., Foley, S. F., Oberti, R., Vannucci, R. & Zanetti, A. (2001). Fractionation of Nb and Ta from Zr and Hf at mantle depths: the role of titanian pargasite and kaersutite. *Journal of Petrology* **42**, 221–232.

Vannucci, R., Piccardo, G. B., Rivalenti, G., Zanetti, A., Rampone, E., Ottolini, L., Oberti, R., Mazzucchelli, M. & Bottazzi, P. (1995). Origin of LREE-depleted amphiboles in the subcontinental mantle. *Geochimica et Cosmochimica Acta* **59**, 1763–1771.

Varela, M. E., Clocchiatti, R., Kurat, G. & Schiano, P. (1999). Silicic glasses in hydrous and anhydrous mantle xenoliths from Western Victoria: at least two different sources. *Chemical Geology* **153**, 151–169.

Vernières, J., Godard, M. & Bodinier, J. L. (1997). A plate model for the simulation of trace element fractionation during partial melting and magma transport in the Earth's upper mantle. *Journal of Geophysical Research* **102**, 24771–24784.

Volker, F. (1990). Geochemie der quartären Vulkanite auf der Ostschulter des Kenia-Rifts. Ph.D. thesis, University of Karlsruhe.

Witt-Eickschen, G., Seck, H. A., Mezger, K., Eggins, S. M. & Altherr, R. (2003). Lithospheric mantle evolution beneath the Eifel (Germany): constraints from Sr–Nd–Pb isotopes and trace element abundances in spinel peridotite and pyroxenite xenoliths. *Journal of Petrology* **44**, 1077–1095.

Woermann, E. & Rosenhauer, M. (1985). Fluid phases and the redox state of the Earth's mantle—extrapolations based on experimental, phase-theoretical and petrological data. *Fortschritte der Mineralogie* **63**, 263–349.

Wood, B. J. & Virgo, D. (1989). Upper mantle oxidation state: ferric iron contents of lherzolite spinels by ^{57}Fe Mössbauer spectroscopy and resultant oxygen fugacities. *Geochimica et Cosmochimica Acta* **53**, 1277–1291.

Woodland, A. B., Kornprobst, J., McPherson, E., Bodinier, J. L. & Menzies, A. (1996). Metasomatic interactions in the lithospheric mantle: petrologic evidence from the Lherz massif, French Pyrenees. *Chemical Geology* **134**, 83–112.

Wulff-Pedersen, E., Neumann, E.-R., Vannucci, R., Bottazzi, P. & Ottolini, L. (1999). Silicic melts produced by reaction between peridotite and infiltrating basaltic melts: ion probe data on glasses and minerals in veined xenoliths from La Palma, Canary Islands. *Contributions to Mineralogy and Petrology* **137**, 59–82.

Yaxley, G. M. & Kemenetsky, V. (1999). *In situ* origin for glass in mantle xenoliths from southeastern Australia: insights from trace element compositions of glasses and metasomatic phases. *Earth and Planetary Science Letters* **172**, 97–109.

Yaxley, G. M., Kamenetsky, V., Green, D. H. & Falloon, T. J. (1997). Glasses in mantle xenoliths from western Victoria, Australia, and their relevance to mantle processes. *Earth and Planetary Science Letters* **148**, 433–446.

Yaxley, G. M., Green, D. H. & Kamenetsky, V. (1998). Carbonatite metasomatism in the southeastern Australian lithosphere. *Journal of Petrology* **39**, 1917–1930.

Zanetti, A., Mazzucchelli, M., Rivalenti, G. & Vannucci, R. (1999). The Finero phlogopite–peridotite massif: an example of subduction-related metasomatism. *Contributions to Mineralogy and Petrology* **134**, 107–122.

Zanetti, Z., Vannucci, R., Bottazzi, P., Oberti, R. & Ottolini, L. (1996). Infiltration metasomatism at Lherz as monitored by systematic ion-microprobe investigations close to a hornblendite vein. *Chemical Geology* **134**, 113–133.

Zinngrebe, E. & Foley, S. F. (1995). Metasomatism in mantle xenoliths from Gees, West Eifel, Germany: evidence for the genesis of calc-alkaline glasses and metasomatic Ca-enrichment. *Contributions to Mineralogy and Petrology* **122**, 79–96.